

Hyperspectral remote sensing of shallow waters: considering environmental noise and bottom intra-class variability for modeling and inversion of water reflectance

Sylvain Jay^{a,*}, Mireille Guillaume^a, Audrey Minghelli^b, Yannick Deville^c, Malik Chamid^{d,e},
Bruno Lafrance^f, Véronique Serfaty^g

^a*Aix Marseille Univ, CNRS, Centrale Marseille, Institut Fresnel, F-13013 Marseille, France*

^b*University of Toulon, CNRS, SeaTech, LSIS laboratory, UMR 7296, 83041 Toulon, France*

^c*Institut de Recherche en Astrophysique et Planétologie (IRAP), Observatoire Midi-Pyrénées, Université de Toulouse, UPS-CNRS-OMP, 31400 Toulouse, France*

^d*Sorbonne Universités, UPMC Univ Paris 06, INSU-CNRS, Laboratoire Atmosphères Milieux Observations Spatiales (LATMOS), 06230 Villefranche sur Mer, France*

^e*Institut Universitaire de France, 75231 Paris Cedex 05, France*

^f*CS Systemes d'Information, 31506 Toulouse Cedex 05, France*

^g*DGA/DS/MRIS, 75509 Paris Cedex 15, France*

Abstract

Hyperspectral remote sensing is now an established tool to determine shallow water properties over large areas, usually by inverting a semi-analytical model of water reflectance. However, various sources of error may make the observed subsurface remote-sensing reflectance deviate from the model, resulting in an increased retrieval error when inverting the model based on classical least-squares fitting. In this paper, we propose a probabilistic forward model of shallow water reflectance variability that describes two of the main sources of error, namely, (1) the environmental noise that includes every source of above-water variability (e.g., sensor noise and rough water surface), and (2) the potentially complex inherent spectral variability of each benthic class through their associated spectral covariance matrix. Based on this probabilistic model, we derive two inversion approaches, namely, MILE (Maximum Likelihood estimation including Environmental noise) and MILEBI (Maximum Likelihood estimation including Environmental noise and Bottom Intra-class variability) that utilize the information contained in the proposed covariance matrices to further constrain the inversion while allowing the observation to differ from the model in the less reliable wavebands. In this paper, MILE and MILEBI are compared with the widely used least-squares (LS) criterion in terms of depth, water clarity and benthic cover retrievals. For these three approaches, we also assess the influence of constraining bottom mixture coefficients to sum to one on

* *Corresponding author.*

estimation results.

The results show that the proposed probabilistic model is a valuable tool to investigate the influence of bottom intra-class variability on subsurface reflectance, e.g., as a function of optical depth or environmental noise. As expected, this influence is critical in very optically shallow waters, and decreases with increasing optical depth. The inversion results obtained from synthetic and airborne data of Quiberon Peninsula, France, show that MILE and MILEBI generally provide better performances than LS. For example, in the case of airborne data with depth ranging from 0.44 to 12.00 m, the bathymetry estimation error decreases by about 32% when using MILE and MILEBI instead of LS. Estimated maps of bottom cover are also more consistent when derived using sum-to-one constrained versions of MILE and MILEBI. MILE is shown to be a simple but powerful method to map simple benthic habitats with negligible influence of intra-class variability. Alternatively, MILEBI is to be preferred if this variability cannot be neglected, since taking bottom covariance matrices into account concurrently with mean reflectance spectra may help the bottom discrimination, e.g., in the presence of overlapping classes. This study thus shows that taking potential sources of error into account through appropriate parameterizations of spectral covariance may be critical to improve the remote sensing of shallow waters, hence making MILE and MILEBI interesting alternatives to LS.

Keywords: Bottom intra-class variability, Environmental noise, Maximum likelihood estimation, Radiative transfer model inversion, Shallow water hyperspectral remote sensing, Spectral covariance

1. Introduction

Optical remote sensing provides an outstanding opportunity to monitor aquatic environments from local to global scales, potentially offering high temporal and spatial resolutions, e.g., as allowed by recent advances in unmanned aerial vehicles or by the Sentinel-2 mission developed by the European Space Agency within the “Copernicus” program (Aschbacher & Milagro-Pérez, 2012; Drusch et al., 2012). The use of such high spatial resolution data (i.e., less than a few dozen meters) is particularly critical for coastal and inland waters, e.g., to map heterogeneous benthic habitats (Mishra et al., 2006; Hedley et al., 2012b), to detect coral bleaching (Andréfouët et al., 2002; Hedley et al., 2012a) or to monitor small lakes and rivers (Joshi & D’Sa, 2015). As compared with the open ocean, coastal and inland waters

11 are generally more complex environments, whose remotely-sensed reflectance may be highly
12 variable due to simultaneous changes in bathymetry, water quality, bottom type, water sur-
13 face and atmospheric conditions. In shallow waters, the decoupling of these effects has been
14 shown to be more accurate when using hyperspectral data instead of multispectral data (Lee
15 & Carder, 2002; Lee et al., 2013). Indeed, a higher number of spectral bands as well as
16 an increased spectral resolution allow reducing confounding effects between optically-active
17 parameters, e.g., by detecting the subtle changes in reflectance that originate from narrow
18 absorption regions potentially present in bottom albedo (Kutser et al., 2003; Hochberg &
19 Atkinson, 2003; Hedley et al., 2012a; Botha et al., 2013).

20

21 In coastal environments, hyperspectral remote sensing methods that allow the simultane-
22 ous retrieval of bathymetry, water quality and benthic cover are usually based on a radiative
23 transfer model that describes how light propagates in water (Mobley, 1994). This inverse
24 problem is generally solved using either look-up tables (LUTs) or iterative optimization
25 (Dekker et al., 2011). In the first case, a spectral library corresponding to different combi-
26 nations of depth, water quality and benthic cover is pre-computed using an exact (Mobley,
27 1994) or approximated (Lee et al., 1998) radiative transfer model. For each image pixel,
28 the measured reflectance is then matched with the closest simulated spectrum in the LUT.
29 CRISTAL (Comprehensive Reflectance Inversion based on Spectrum matching and TABLE
30 Lookup) (Mobley et al., 2005) and ALLUT (Adaptive Linearized Look-Up Trees) (Hedley
31 et al., 2009) as denoted by Dekker et al. (2011) are examples of such approaches. The inverse
32 problem can also be solved by numerically optimizing a cost function that relates measured
33 and simulated reflectance spectra. In this case, the forward model used for simulation has
34 to be sufficiently fast to permit multiple runs for each image pixel. To this end, a number of
35 analytical and semi-analytical models have been developed under various assumptions and
36 water types (Maritorena et al., 1994; Lee et al., 1998; Albert & Mobley, 2003). These models
37 approximate the radiative transfer equation and generally simulate the reflectance of shal-
38 low waters as a function of sun-sensor geometry, depth, bottom albedo and water-column
39 inherent optical properties (i.e., absorption and scattering properties of the water column).
40 Note that, whenever possible, the latter can further be related to specific inherent optical

41 properties and concentrations of optically-active water constituents (Brando et al., 2009).

42

43 Due to its accurate performance and simplicity, the Euclidean distance has generally been
44 used to assess the goodness-of-fit between the observation and the model, either when using
45 LUTs (Mobley et al., 2005; Hedley et al., 2009, 2012a) or iterative optimization (Lee et al.,
46 1999, 2001; Lee & Carder, 2002; Albert & Gege, 2006; Klonowski et al., 2007; Dekker et al.,
47 2011; Jay et al., 2012; Giardino et al., 2012; Garcia et al., 2014a; McKinna et al., 2015; Jay
48 & Guillaume, 2016). Note that in the case of iterative optimization, the use of Euclidean dis-
49 tance for model inversion corresponds to nonlinear unweighted least-squares fitting. However,
50 this cost function does not fully consider the information contained in the reflectance data.
51 In particular, it does not utilize spectral covariance (i.e., covariance between wavebands), yet
52 such knowledge of the data structure may be useful to improve the retrieval accuracy due to
53 the non-negligible correlation between hyperspectral bands (Gillis et al., 2013).

54

55 Importantly, as the least-squares method tries to find the best possible fit between the
56 observation and the model, it is not designed to handle possible deviations between them.
57 For example, the “environmental noise equivalent reflectance difference” (Brando & Dekker,
58 2003) (hereafter called environmental noise and denoted $NE\Delta r_E$) may lead the measured
59 subsurface reflectance to strongly differ from the modeled one. For a given spectral band,
60 $NE\Delta r_E$ corresponds to the reflectance standard deviation as estimated over an “as homoge-
61 neous as possible” water area. As a result, it not only takes into account the sensor noise, but
62 also scene-specific above-water variability, including atmospheric variability, effects related
63 to the rough water surface, refractions of diffuse and direct sunlight, and residuals from im-
64 perfect atmospheric, air-water interface and sun glint corrections (Brando & Dekker, 2003;
65 Brando et al., 2009; Botha et al., 2013). To consider such errors within model inversion,
66 Brando et al. (2009) and Botha et al. (2013) have weighted the contribution of each wave-
67 band according to the inverse of $NE\Delta r_E$. In doing so, the influence of the noisiest and least
68 accurate spectral bands is reduced, which lowers the estimation variance.

69

70 Another important source of error between the measured and simulated spectra is the

71 inherent spectral variability of each considered benthic class. Based on PlanarRad simu-
72 lations and a comprehensive bottom spectral library, Hedley et al. (2012b) have actually
73 demonstrated that this is one of the primary limiting factors for benthic mapping purposes
74 (whereas sensor noise is only a minor factor). Indeed, while a single mean reflectance spec-
75 trum is generally used to characterize the spectral response of each benthic class, many
76 authors show that such intrinsic variability may sometimes be greater than the mean re-
77 flectance itself, either at the local or global scales (Hochberg et al., 2003; Mobley et al., 2005;
78 Hedley et al., 2012b; Petit et al., 2017). Therefore, this variability may strongly affect the re-
79 trieval accuracy if it is not (or not properly) taken into account during the inversion process.
80 To this end, assuming that the bottom reflectance spectrum only varies according to a single
81 multiplicative factor across all the wavebands, several authors have proposed to estimate this
82 factor for each possible substrate (Lee et al., 1999; Fearn et al., 2011; Garcia et al., 2014b;
83 Petit et al., 2017). Under the same assumption, using the Spectral Angle Mapper (SAM) as
84 a cost function may also decrease the detrimental influence of bottom intra-class variability,
85 since the SAM is insensitive to variations in the global reflectance magnitude (Brando et al.,
86 2009; Botha et al., 2013; Petit et al., 2017). However, this spectral variability cannot always
87 be reliably represented using a single multiplicative factor (Hochberg et al., 2003; Hedley
88 et al., 2012b), thus making the development of alternative inversion methods highly desirable.

89

90 In this study, we first propose a realistic probabilistic model of shallow water reflectance
91 variability based on the semi-analytical model of Lee et al. (1998) and that fully describes
92 the influences of environmental noise and bottom intra-class variability. Both sources of
93 error are considered to be Gaussian and characterized by a mean vector and a spectral
94 covariance matrix. Then, using this modeling, we develop two new inversion approaches
95 based on maximum likelihood estimation that enable a pixelwise retrieval of all optically-
96 active parameters, i.e., bathymetry, water clarity parameters and benthic cover. These two
97 approaches are compared with the classical least-squares method using both simulated and
98 airborne data.

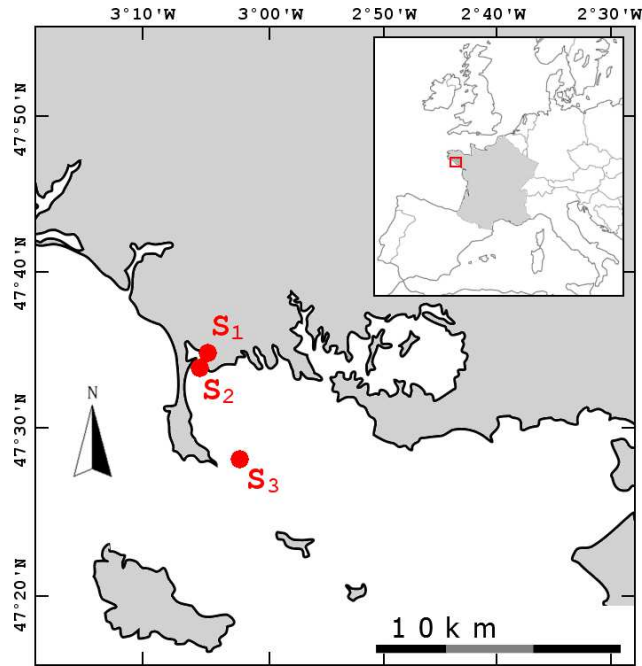


Figure 1: Location of the three study sites S_1 , S_2 and S_3 .

99 2. Data

100 2.1. Study area

101 As shown in Fig. 1, the overall study area is located in the Quiberon Bay on the French
 102 west coast (around $47^{\circ}31'N$, $3^{\circ}05'W$). Three sites (hereafter denoted S_1 , S_2 and S_3) were
 103 chosen in order to include a large bathymetric range and various bottom covers. Site S_1 and
 104 Site S_2 are located near the shore in the Bay of Plouharnel ($47^{\circ}34'46''N$, $3^{\circ}06'24''W$), and
 105 are characterized by relatively shallow waters (less than 5 m at the time of acquisitions) and
 106 heterogeneous bottom covers including sand, brown and green algae, seagrasses and oyster
 107 farming structures. Site S_3 is located a few kilometers away from the Quiberon peninsula
 108 ($47^{\circ}28'11''N$, $3^{\circ}02'18''W$) and is characterized by a large bathymetric range (from 4 to 12 m
 109 at the time of acquisitions) and a nearly uniform sandy bottom.

110 2.2. Image acquisition and preprocessing

111 Eight hyperspectral images were acquired on September 14-18, 2010 around solar noon
 112 (the solar zenith angle being close to 50°) using an airborne Hypspx VNIR-1600 push-broom
 113 camera (Norsk Elektro Optikk, Norway). The flight altitude was 650 m, resulting in a 0.5 m
 114 spatial resolution. The camera acquired successive lines of 1600 pixels and 160 spectral bands

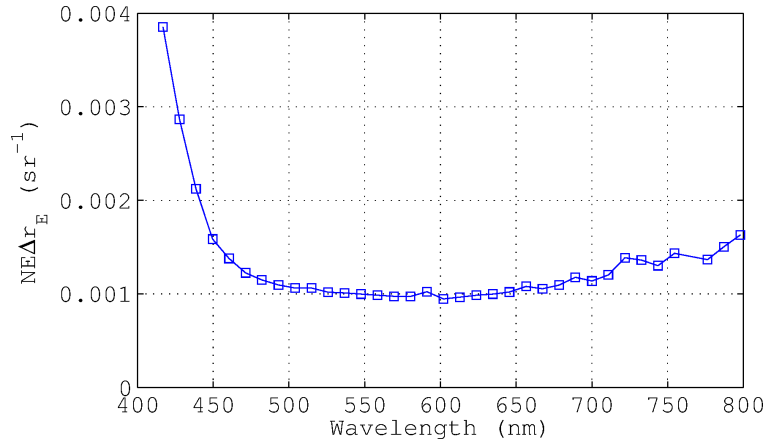


Figure 2: Environmental noise as measured on September 18, 2010.

115 ranging from 410 to 987 nm. The spectral sampling interval and full width at half maxi-
 116 mum were 3.7 nm and 4.5 nm respectively. Only 105 bands in the 410-800 nm domain were
 117 kept when removing the strong water and oxygen absorption regions. Further, a three-band
 118 aggregate was performed similarly to the PRISM instrument developed by the Jet Propul-
 119 sion Laboratory (Mouroulis et al., 2014), therefore leading to a 11 nm sampling interval (35
 120 bands). This allows us to enhance the signal-to-noise ratio while keeping similar estimation
 121 results (Hochberg & Atkinson, 2003; Garcia et al., 2015).

122

123 The at-sensor radiance images were geometrically corrected, geolocated, and converted
 124 into above-surface reflectance using the ATCOR atmospheric correction (Richter, 2012) (for
 125 further details about these corrections, please see Jay & Guillaume (2016)). Sun glint (Hedley
 126 et al., 2005) and the air/water interface (Lee et al., 1999) were corrected in order to finally
 127 obtain the subsurface remote-sensing reflectance $r(\lambda)$ (in sr^{-1}). For each day of acquisition,
 128 the environmental noise $\text{NE}\Delta r_E$ (in sr^{-1}) (Brando & Dekker, 2003) was estimated over
 129 optically deep waters according to the methodology proposed by Wettle et al. (2004). As
 130 shown in Fig. 2, its spectral shape is similar to those obtained in previous studies (Brando
 131 et al., 2009; Wettle et al., 2004), i.e., $\text{NE}\Delta r_E$ is nearly constant across all wavebands and
 132 mainly increases in the blue domain, where the sensitivity of the CCD sensor is the lowest
 133 and spectral variations in incident light are the strongest.

134 *2.3. Data used for depth and phytoplankton concentration estimations*

135 The eight hyperspectral images were used to evaluate the accuracy of bathymetry re-
136 trieval. For each image, the depth was only known in a few 6×6 m² flat sandy-bottom areas
137 thanks to sonar measurements and a tide model. A total of 14 validation points (depth
138 ranging from 0.44 to 12 m) were therefore available to assess the accuracy of bathymetry
139 estimation.

140 In addition, phytoplankton concentration was also measured concurrently with most airborne
141 acquisitions in Site S₃. To do so, water samples were collected at the surface and bottom
142 (whose depth ranged from 4.70 to 12 m) levels to better account for a possible vertical gra-
143 dient in phytoplankton concentration. Chlorophyll-*a* and pheopigment concentrations were
144 measured according to the French standard NF T 90117 (AFNOR, December 1999). Surface
145 and bottom phytoplankton concentrations were then given by the sum of chlorophyll-*a* and
146 pheopigment concentrations, and averaged so as to obtain a single measurement for each
147 sampled area. These mean values were finally used to derive the absorption coefficient of
148 phytoplankton at 440 nm (denoted P , in m⁻¹) similarly to Lee et al. (1999). In total, 8 vali-
149 dation points (phytoplankton concentration ranging from 1.25 to 1.95 $\mu\text{g.L}^{-1}$, corresponding
150 to P ranging from 0.069 to 0.093 m⁻¹) were available (still over 6×6 m² flat sandy-bottom
151 areas within which P was assumed to be homogeneous).

152 Note that no data were available to assess the retrievals of the other optically-active wa-
153 ter constituents, namely, colored dissolved organic and detrital matter as well as suspended
154 matter (see Section 3.1.1).

155 *2.4. Data used for bottom cover estimation*

156 The above eight images were also used to assess bottom cover estimation over the 14
157 6×6 m² flat sandy-bottom areas of known depth. In addition, one of these images was
158 used to assess the tested methods over more complex bottom covers (Fig. 3). This image
159 was acquired over a 0.22 km² area located in site S₂. This shallow area was part of a large
160 oyster farming area and was thus relatively heterogeneous, both in terms of bottom cover and
161 bathymetry (the depth ranged from about 1 m in the left-hand part to 5 m in the top-right
162 part, with locally sharp changes in bathymetry due to the presence of oyster racks). Various

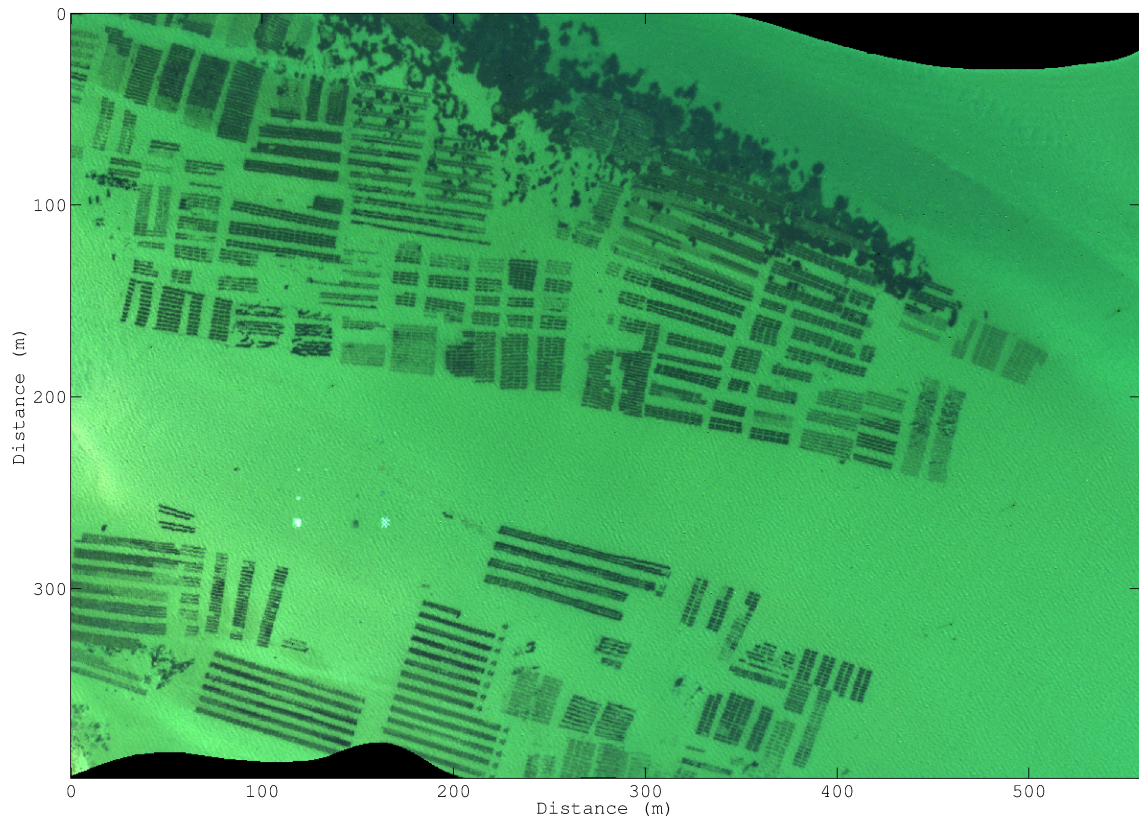


Figure 3: True color composite image derived from the deglinted subsurface remote-sensing reflectance image that was used to assess the bottom cover estimation (note that the dynamic range of the image was enhanced by multiplying every pixel by a factor of 10).

163 bottom types were identified in this area. Numerous oyster racks were present on a mostly
 164 sandy bottom. Some of these wooden structures were empty (e.g., in the upper left part of
 165 the image), but most of them were full of oyster bags at the time of acquisition. Depending
 166 on when these bags had been put on racks, they could partly or completely be covered with
 167 green algae and/or brown algae. Lastly, there was a large seagrass meadow in the upper right
 168 part of the image, as well as small patches of brown algae irregularly distributed within the
 169 image (e.g., between oyster racks in the lower left part). Note that the colored tarpaulins
 170 present on the left-hand side (in the middle of which depth was 2.83 m) were ignored in this
 171 study.

172 For each bottom class and based on expert knowledge, numerous endmember spectra were
 173 extracted from supplementary hyperspectral images acquired over the neighboring zones in
 174 Site S₂ during low tide (Fig. 4). It is worth mentioning that, due to intra-class variability
 175 and because these zones are a few hundred meters to a dozen kilometers from the zones used
 176 to assess the inversion methods (Fig. 1), the extracted endmember spectra may not perfectly

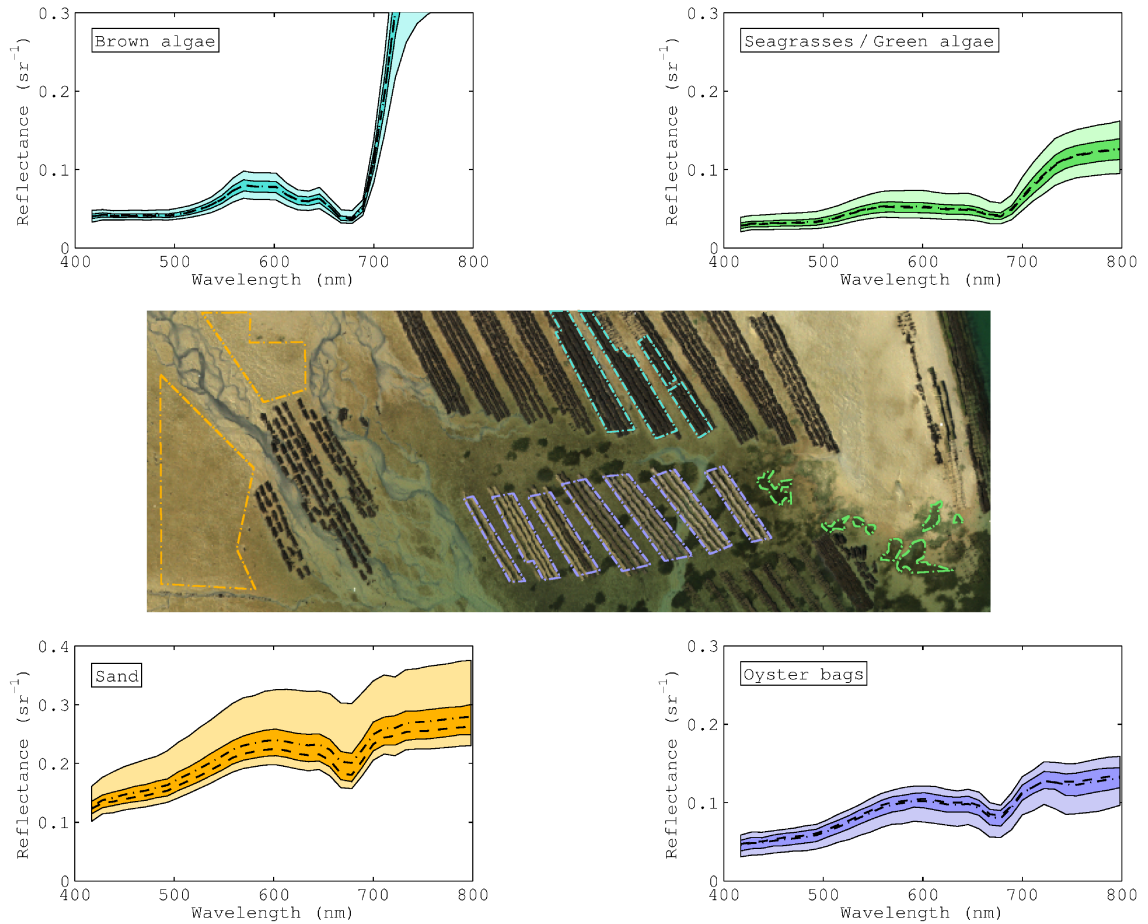


Figure 4: Reflectance distributions of sand, oyster bag, seagrass/green algae and brown algae classes as estimated from the areas emphasized in the airborne hyperspectral image shown in the middle. For each plot, the darkest and brightest shades correspond to the 25-75% and 5-95% quantiles resp., whereas the median and mean spectra are indicated by dashed and dash-dot lines resp..

177 match those encountered in the whole study area. Selecting reflectance spectra of emerged
 178 substrates directly from the remote-sensing images allowed us to avoid potential issues of
 179 intercalibration between airborne and ground-based sensors. However, note that, since empty
 180 wooden structures were too thin to fill entirely the $0.5 \times 0.5 \text{ m}^2$ pixels of hyperspectral images,
 181 they were not included as a possible endmember. Further, green algae and seagrasses were
 182 grouped into a single class corresponding to green vegetation elements. Four bottom classes
 183 were thus used, namely sand, oyster bags, brown algae and seagrasses/green algae (note that
 184 these surfaces were assumed to be Lambertian). The corresponding reflectance distributions
 185 were estimated based on 150 to 3,000 image spectra, and all show some intra-class variability
 186 around the mean reflectance spectra (Fig. 4). Such variability may be due, e.g., to the bottom
 187 chemistry itself (e.g., variations in chlorophyll content in seagrasses/green algae) or to the
 188 bottom 3-D arrangement that may make the illumination conditions within the surface highly

189 variable (Manolakis et al., 2003). Given the similar magnitudes of brown alga, seagrass/green
 190 alga and, to a lesser extent, oyster bag mean reflectance spectra, such variability potentially
 191 makes the identification of these three partially overlapping classes quite difficult.

192 3. Methodology

193 3.1. Forward modeling of subsurface remote-sensing reflectance

194 3.1.1. Bio-optical modeling

195 In this study, we use the semi-analytical model $\tilde{r}(\lambda)$ developed by Lee et al. (1998, 1999)
 196 to express the subsurface remote-sensing reflectance as measured from nadir as a function
 197 of depth H (in m), bottom albedo $\rho_b(\lambda)$ (unitless), total absorption and backscattering
 198 properties of the water column $a(\lambda)$ and $b_b(\lambda)$ resp. (in m^{-1}), and subsurface solar zenith
 199 angle θ_s (in $^\circ$):

$$200 \quad \tilde{r}(\lambda) = r_\infty(\lambda) \left(1 - e^{-(k_d(\lambda) + k_u^c(\lambda))H}\right) + \frac{\rho_b(\lambda)}{\pi} e^{-(k_d(\lambda) + k_u^b(\lambda))H} \quad (1)$$

201 where the subsurface remote-sensing reflectance of optically-deep water $r_\infty(\lambda)$ (in sr^{-1}) and
 202 attenuation coefficients $k_d(\lambda)$, $k_u^c(\lambda)$ and $k_u^b(\lambda)$ (in m^{-1}) are related to $a(\lambda)$, $b_b(\lambda)$ and θ_s by:

$$203 \quad r_\infty(\lambda) = \left(0.084 + 0.17 \frac{b_b(\lambda)}{a(\lambda) + b_b(\lambda)}\right) \frac{b_b(\lambda)}{a(\lambda) + b_b(\lambda)} \quad (2)$$

$$204 \quad k_d(\lambda) = \frac{a(\lambda) + b_b(\lambda)}{\cos \theta_s} \quad (3)$$

$$205 \quad k_u^b(\lambda) = 1.04(a(\lambda) + b_b(\lambda)) \left(1 + 5.4 \frac{b_b(\lambda)}{a(\lambda) + b_b(\lambda)}\right)^{0.5} \quad (4)$$

$$206 \quad k_u^c(\lambda) = 1.03(a(\lambda) + b_b(\lambda)) \left(1 + 2.4 \frac{b_b(\lambda)}{a(\lambda) + b_b(\lambda)}\right)^{0.5}. \quad (5)$$

207 Eq. (1) to Eq. (5) have been used and validated in numerous studies dealing with shallow
 208 water remote sensing over a wide range of coastal waters (Lee et al., 1999, 2001; Klonowski
 209 et al., 2007; Goodman et al., 2008; Brando et al., 2009; Hedley et al., 2009; Dekker et al.,
 210 2011; Fearnas et al., 2011; Garcia et al., 2014a; Jay & Guillaume, 2014; McKinna et al.,
 211 2015; Jay & Guillaume, 2016; Petit et al., 2017). In the absence of *in-situ* measurements of
 212 inherent optical properties to develop a site-specific bio-optical model, the total absorption

213 and backscattering coefficients are given by the sum of the contributions of optically-active
 214 water constituents and parameterized according to the generic expressions of Lee et al. (1998)
 215 and Dekker et al. (2011):

$$216 \quad a(\lambda) = a_w(\lambda) + [a_0(\lambda) + a_1(\lambda) \ln P] P + Ge^{-0.015(\lambda-440)} \quad (6)$$

$$217 \quad b_b(\lambda) = b_{b,w}(\lambda) + X \left(\frac{550}{\lambda} \right)^{0.5} \quad (7)$$

218 where $a_w(\lambda)$ and $b_{b,w}(\lambda)$ (in m^{-1}) are the pure water absorption and backscattering coeffi-
 219 cients (Buiteveld et al., 1994; Morel, 1974), $a_0(\lambda)$ and $a_1(\lambda)$ (unitless) are empirical spectra
 220 tabulated by Lee et al. (1998), P (in m^{-1}) is the absorption coefficient of phytoplankton at
 221 440 nm, G (in m^{-1}) is the absorption coefficient of colored dissolved organic and detrital
 222 matter at 440 nm, and X (in m^{-1}) is the particle backscattering coefficient at 550 nm. The
 223 above parameterizations of absorption coefficients of phytoplankton and colored dissolved
 224 organic and detrital matter have been shown to be sufficiently accurate over a wide range
 225 of coastal waters (Lee et al., 1999, 2001; Lee & Carder, 2002; Goodman et al., 2008; Hedley
 226 et al., 2009; Dekker et al., 2011; Hedley et al., 2012a; Jay & Guillaume, 2014, 2016). Note
 227 also that the power law exponent used to model particle backscattering was set to -0.5, which
 228 is adequate for normal to more turbid coastal waters (Lee et al., 2001).

229 In order to accurately model the response of oyster racks (which are relatively thin com-
 230 pared to the $0.5 \times 0.5 \text{ m}^2$ pixel size) while appropriately limiting the number of unknowns
 231 and, therefore, the estimation uncertainty, the bottom albedo is parameterized using a linear
 232 combination of two pure substrates similarly to Brando et al. (2009) and Hedley et al. (2009):

$$233 \quad \rho_b(\lambda) = B_1 \rho_{b,1}(\lambda) + B_2 \rho_{b,2}(\lambda) \quad (8)$$

234 where $\rho_{b,1}(\lambda)$ and $\rho_{b,2}(\lambda)$ are two known substrate albedos (e.g., obtained from ground-based
 235 measurements or a generic spectral library). The scalars B_1 and B_2 (unitless) may represent
 236 the fractional covers of both substrates within the considered pixel, so in this case, only one
 237 bottom coefficient B is required, i.e., $B_1 = B$, $B_2 = 1 - B$ and $0 \leq B \leq 1$ (Klonowski et al.,
 238 2007; Goodman & Ustin, 2007; Brando et al., 2009; Hedley et al., 2009, 2012a). Alterna-

239 tively, Fearn et al. (2011) and Garcia et al. (2014b) used a mixture of benthic reflectances
 240 normalized at 550 nm, and they estimated the relative brightness of each substrate without
 241 imposing any constraint on the mixture coefficients to be retrieved. In this case, a single
 242 multiplicative factor is used to model both the fractional cover and the brightness (or magni-
 243 tude) of each substrate. Although the sum-to-one constraint applies for the fractional cover,
 244 the brightness of substrate $\rho_{b,1}$ is independent from that of substrate $\rho_{b,2}$. As a result, the
 245 mixture coefficients B_1 and B_2 are independent and do not necessarily sum to one. It is worth
 246 noting that, even though such a modeling enables the magnitudes of $\rho_{b,1}$ and $\rho_{b,2}$ to vary,
 247 it also adds an extra degree of freedom during the inversion process. This may increase the
 248 estimation noise and require post-processing steps in order to smooth estimated maps, e.g.,
 249 using median filtering (Fearn et al., 2011). In the following, we test these two approaches
 250 in order to assess the impact of the sum-to-one constraint on estimation performance.

251 3.1.2. Probabilistic modeling

252 As widely accepted in the community (Jay & Guillaume, 2011; Hedley et al., 2012a;
 253 Jay et al., 2012; Gillis et al., 2013; Garcia et al., 2014b; Jay & Guillaume, 2014; Knudby
 254 et al., 2016), the measured subsurface remote-sensing reflectance, denoted in vector form
 255 $\mathbf{r} = [r(\lambda_1), \dots, r(\lambda_L)]^t$ (where L is the number of wavebands), is assumed to follow a mul-
 256 tivariate Gaussian distribution with mean $\boldsymbol{\mu} = \mathbb{E}[\mathbf{r}]$ and spectral covariance matrix $\boldsymbol{\Gamma} =$
 257 $\mathbb{E}[(\mathbf{r} - \mathbb{E}(\mathbf{r}))(\mathbf{r} - \mathbb{E}(\mathbf{r}))^t]$. The mean vector is parameterized using the bio-optical model
 258 presented in Section 3.1.1, which may be written in matrix notation as

$$259 \quad \boldsymbol{\mu}(\boldsymbol{\Delta}) = (\mathbb{I} - \mathbf{K}_c)\mathbf{r}_\infty + \mathbf{K}_b \left(B_1 \frac{\boldsymbol{\rho}_{b,1}}{\pi} + B_2 \frac{\boldsymbol{\rho}_{b,2}}{\pi} \right) \quad (9)$$

260 where $\boldsymbol{\Delta} = [H, P, G, X, B_1, B_2]^t$, $\mathbf{r}_\infty = [r_\infty(\lambda_1), \dots, r_\infty(\lambda_L)]^t$, \mathbb{I} is the $L \times L$ identity matrix,
 261 $\mathbf{K}_c = \text{diag} \left[e^{-(k_d(\lambda_i) + k_u^c(\lambda_i))H} \right]_{i \in \llbracket 1; L \rrbracket}$, $\mathbf{K}_b = \text{diag} \left[e^{-(k_d(\lambda_i) + k_u^b(\lambda_i))H} \right]_{i \in \llbracket 1; L \rrbracket}$, and $\boldsymbol{\rho}_{b,i} = [\rho_{b,i}(\lambda_1), \dots, \rho_{b,i}(\lambda_L)]^t$.

262
 263 The different sources of deviations between the measured and simulated spectra can be
 264 modeled via an appropriate parameterization of $\boldsymbol{\Gamma}$. In the probabilistic modeling subse-
 265 quently used within the proposed MILE (Maximum Likelihood estimation including En-

266 vironmental noise) inversion method (Section 3.2), we assume that the random variability
 267 around mean $\boldsymbol{\mu}(\boldsymbol{\Delta})$ can be described using the full spectral covariance matrix of the envi-
 268 ronmental noise, $\boldsymbol{\Gamma}_{surf}$, similarly to Hedley et al. (2012a), Garcia et al. (2014b) and Knudby
 269 et al. (2016). The subsurface remote-sensing reflectance is then modeled as

$$270 \quad \mathbf{r} = \left[(\mathbb{I} - \mathbf{K}_c) \mathbf{r}_\infty + \mathbf{K}_b \left(B_1 \frac{\boldsymbol{\rho}_{b,1}}{\pi} + B_2 \frac{\boldsymbol{\rho}_{b,2}}{\pi} \right) \right] + \mathbf{n}_{surf} \quad (10)$$

271 where the random vector \mathbf{n}_{surf} follows a multivariate Gaussian distribution with zero mean
 272 and covariance matrix $\boldsymbol{\Gamma}_{surf}$. Note that, in real scenarios, $\boldsymbol{\Gamma}_{surf}$ can be estimated over opti-
 273 cally deep waters similarly to $\text{NE}\Delta r_E$.

274

275 However, Eq. (10) only allows the bottom remote-sensing reflectances $(\boldsymbol{\rho}_{b,1}/\pi)$ and $(\boldsymbol{\rho}_{b,2}/\pi)$
 276 to vary according to the multiplicative factors B_1 and B_2 . As an alternative to this usual
 277 bottom modeling, the proposed MILEBI (MaxImum Likelihood estimation including Envi-
 278 ronmental noise and Bottom Intra-class variability) probabilistic modeling uses a multivariate
 279 Gaussian distribution to describe the reflectance inherent variability of each benthic class.
 280 Due to the compromise offered between accuracy and mathematical tractability, the Gaus-
 281 sian modeling has been widely used to develop hyperspectral remote-sensing algorithms that
 282 must take into account the spread of each class of materials (and therefore potential overlaps
 283 between these classes) to obtain good performances, e.g., classification and target detection
 284 algorithms (Manolakis et al., 2003; Melgani & Bruzzone, 2004; Palmason et al., 2005). Pre-
 285 liminary tests (not shown here for the sake of brevity) demonstrated that, except for a small
 286 minority of samples corresponding to extreme data points, the bottom intra-class variabil-
 287 ities presented in Fig. 4 could indeed be reliably represented using multivariate Gaussian
 288 distributions. In this case, the subsurface remote-sensing reflectance can be modeled as

$$289 \quad \mathbf{r} = \left\{ (\mathbb{I} - \mathbf{K}_c) \mathbf{r}_\infty + \mathbf{K}_b \left[B_1 (\boldsymbol{\mu}_{b,1} + \mathbf{n}_{b,1}) + B_2 (\boldsymbol{\mu}_{b,2} + \mathbf{n}_{b,2}) \right] \right\} + \mathbf{n}_{surf} \quad (11)$$

290 where $\boldsymbol{\mu}_{b,i}$ is the mean remote-sensing reflectance spectrum of bottom class i and $\mathbf{n}_{b,i}$ follows
 291 a multivariate Gaussian distribution with zero mean and covariance matrix $\boldsymbol{\Gamma}_{b,i}$. Separating

292 deterministic terms from random terms in Eq. (11) leads to

$$293 \quad \mathbf{r} = [(\mathbf{I} - \mathbf{K}_c)\mathbf{r}_\infty + \mathbf{K}_b (B_1\boldsymbol{\mu}_{b,1} + B_2\boldsymbol{\mu}_{b,2})] + [\mathbf{n}_{surf} + \mathbf{K}_b(B_1\mathbf{n}_{b,1} + B_2\mathbf{n}_{b,2})]. \quad (12)$$

294 The corresponding total covariance matrix is obtained by applying $\boldsymbol{\Gamma} = \mathbb{E}[(\mathbf{r} - \mathbb{E}(\mathbf{r}))(\mathbf{r} - \mathbb{E}(\mathbf{r}))^t]$
 295 to Eq. (12) and by assuming that $\mathbf{n}_{b,1}$, $\mathbf{n}_{b,2}$ and \mathbf{n}_{surf} are independent:

$$296 \quad \boldsymbol{\Gamma}(\boldsymbol{\Delta}) = \mathbf{K}_b [B_1^2\boldsymbol{\Gamma}_{b,1} + B_2^2\boldsymbol{\Gamma}_{b,2}] \mathbf{K}_b + \boldsymbol{\Gamma}_{surf}. \quad (13)$$

297 In Eq. (12), possible deviations between the observed subsurface remote-sensing reflectance
 298 \mathbf{r} and the model (left-hand term of the sum) are not only due to the environmental noise,
 299 but also to the intrinsic spectral variability of each benthic class. As expected, for the i^{th}
 300 class, the influence of this variability is proportional to B_i , and becomes negligible when
 301 depth and/or turbidity increase(s) (because of progressive attenuation by \mathbf{K}_b). Also, if $\boldsymbol{\Gamma}_{b,1}$
 302 and $\boldsymbol{\Gamma}_{b,2}$ perfectly describe the bottom intrinsic variabilities, the parameters B_1 and B_2 only
 303 represent fractional covers, so the sum-to-one constraint applies. In this case, the MILEBI
 304 probabilistic modeling disentangles the fractional cover (which is taken into account by a
 305 single multiplicative factor $B = B_1 = 1 - B_2$) from intra-class variabilities (which are taken
 306 into account through the bottom covariance matrices $\boldsymbol{\Gamma}_{b,1}$ and $\boldsymbol{\Gamma}_{b,2}$), which is not possible
 307 when using Eq. (10). Alternatively, relaxing the sum-to-one constraint may allow potential
 308 deviations from the assumed Gaussian modeling.

309 *3.2. Inversion methods*

310 In this study, various inversion methods are derived based on the above two probabilis-
 311 tic models of shallow water reflectance variability. All these inversion methods consist in
 312 maximizing the likelihood of observing \mathbf{r} given the set $\boldsymbol{\Delta}$ of water column parameters to be
 313 estimated. Under the Gaussian assumption, the likelihood is defined as

$$314 \quad P(\mathbf{r}|\boldsymbol{\Delta}) = [(2\pi)^L |\boldsymbol{\Gamma}(\boldsymbol{\Delta})|]^{-1/2} e^{-\frac{1}{2}(\mathbf{r} - \boldsymbol{\mu}(\boldsymbol{\Delta}))^t \boldsymbol{\Gamma}(\boldsymbol{\Delta})^{-1} (\mathbf{r} - \boldsymbol{\mu}(\boldsymbol{\Delta}))}. \quad (14)$$

315 The maximum likelihood estimate $\widehat{\Delta}_{ML}(\mathbf{r})$ is the value of Δ that maximizes the likelihood:

$$316 \quad \widehat{\Delta}_{ML}(\mathbf{r}) = \underset{\Delta}{\operatorname{argmax}} P(\mathbf{r}|\Delta). \quad (15)$$

317 In Eq. (14), the mean vector $\boldsymbol{\mu}(\Delta)$ is given by Eq. (9) for every tested inversion method.

318 The main difference between the methods actually lies in the parameterization of $\boldsymbol{\Gamma}(\Delta)$.

319 In MILE, $\boldsymbol{\Gamma}(\Delta) = \boldsymbol{\Gamma}_{surf}$ does not depend on Δ since it only characterizes the above-water

320 variability. Eq. (14) can thus be simplified, and the MILE estimate $\widehat{\Delta}_{MILE}(\mathbf{r})$ is given by

321 the minimum Mahalanobis distance between the measured and simulated spectra:

$$322 \quad \widehat{\Delta}_{MILE}(\mathbf{r}) = \underset{\Delta}{\operatorname{argmin}} (\mathbf{r} - \boldsymbol{\mu}(\Delta))^t \boldsymbol{\Gamma}_{surf}^{-1} (\mathbf{r} - \boldsymbol{\mu}(\Delta)). \quad (16)$$

323 In MILEBI, $\boldsymbol{\Gamma}(\Delta)$ depends on Δ , so Eq. (14) cannot be further simplified:

$$324 \quad \widehat{\Delta}_{MILEBI}(\mathbf{r}) = \underset{\Delta}{\operatorname{argmax}} \left\{ [(2\pi)^L |\boldsymbol{\Gamma}(\Delta)|]^{-1/2} e^{-\frac{1}{2}(\mathbf{r} - \boldsymbol{\mu}(\Delta))^t \boldsymbol{\Gamma}(\Delta)^{-1} (\mathbf{r} - \boldsymbol{\mu}(\Delta))} \right\} \quad (17)$$

325 where $\boldsymbol{\Gamma}(\Delta)$ is given by Eq. (13).

326 In this paper, MILE and MILEBI are compared to the widely used least-squares (LS) method.

327 Note that the LS estimate can also be obtained by maximizing the likelihood in Eq. (14),

328 taking $\boldsymbol{\Gamma} = \sigma^2 \boldsymbol{I}$ where σ is a positive real number and \boldsymbol{I} is the $L \times L$ identity matrix (i.e.,

329 uncertainties of all spectral bands are assumed to be uncorrelated and of equal variances).

330 The LS estimate $\widehat{\Delta}_{LS}(\mathbf{r})$ is given by the minimum Euclidean distance between the measured

331 and simulated spectra:

$$332 \quad \widehat{\Delta}_{LS}(\mathbf{r}) = \underset{\Delta}{\operatorname{argmin}} (\mathbf{r} - \boldsymbol{\mu}(\Delta))^t (\mathbf{r} - \boldsymbol{\mu}(\Delta)). \quad (18)$$

333 Comparing Eq. (16), Eq. (17) and Eq. (18) shows that, unlike LS, MILE and MILEBI utilize

334 the information contained in the spectral covariance matrix to further constrain the inversion.

335 In addition, both methods allow some deviations between the measured and simulated spectra

336 by giving the less reliable wavebands little weights in the cost function. For MILE, these are

337 located in the domains of strong environmental noise. For MILEBI, these wavebands not

Table 1: Methods compared in this study and derived from the likelihood function presented in Eq. (14). Subscript “S21” indicates the use of the sum-to-one constraint.

Method	Δ	$\mu(\Delta)$	$\Gamma(\Delta)$
LS _{S21}	$[H, P, G, X, B]$	$(\mathbb{I} - \mathbf{K}_c)r_\infty + \mathbf{K}_b \left(B \frac{\rho_{b,1}}{\pi} + (1-B) \frac{\rho_{b,2}}{\pi} \right)$	$\sigma^2 \mathbb{I}$
MILE _{S21}	$[H, P, G, X, B]$	$(\mathbb{I} - \mathbf{K}_c)r_\infty + \mathbf{K}_b \left(B \frac{\rho_{b,1}}{\pi} + (1-B) \frac{\rho_{b,2}}{\pi} \right)$	Γ_{surf}
MILEBI _{S21}	$[H, P, G, X, B]$	$(\mathbb{I} - \mathbf{K}_c)r_\infty + \mathbf{K}_b \left(B \frac{\rho_{b,1}}{\pi} + (1-B) \frac{\rho_{b,2}}{\pi} \right)$	$\mathbf{K}_b [B^2 \Gamma_{b,1} + (1-B)^2 \Gamma_{b,2}] \mathbf{K}_b + \Gamma_{surf}$
LS	$[H, P, G, X, B_1, B_2]$	$(\mathbb{I} - \mathbf{K}_c)r_\infty + \mathbf{K}_b \left(B_1 \frac{\rho_{b,1}}{\pi} + B_2 \frac{\rho_{b,2}}{\pi} \right)$	$\sigma^2 \mathbb{I}$
MILE	$[H, P, G, X, B_1, B_2]$	$(\mathbb{I} - \mathbf{K}_c)r_\infty + \mathbf{K}_b \left(B_1 \frac{\rho_{b,1}}{\pi} + B_2 \frac{\rho_{b,2}}{\pi} \right)$	Γ_{surf}
MILEBI	$[H, P, G, X, B_1, B_2]$	$(\mathbb{I} - \mathbf{K}_c)r_\infty + \mathbf{K}_b \left(B_1 \frac{\rho_{b,1}}{\pi} + B_2 \frac{\rho_{b,2}}{\pi} \right)$	$\mathbf{K}_b [B_1^2 \Gamma_{b,1} + B_2^2 \Gamma_{b,2}] \mathbf{K}_b + \Gamma_{surf}$

338 only correspond to the domains of strong environmental noise, but also to the domains of
339 strong bottom intrinsic variabilities.

340 Implementing MILE, MILEBI and LS with or without the sum-to-one constraint on bottom
341 mixture coefficients results in the six methods summarized in Table 1. Note that other
342 cost functions, such as SAM or least-squares on spectral derivative (Brando et al., 2009;
343 Botha et al., 2013; Petit et al., 2017), could also be tested, since, for example, SAM may
344 provide more accurate bathymetry retrieval than LS (Petit et al., 2017). We, however, only
345 compared MILE, MILEBI and LS (1) in order to focus primarily on the influence of $\Gamma(\Delta)$
346 parameterization on the inversion, and (2) because LS generally offers a better tradeoff than
347 SAM and least-squares on spectral derivative for accurately retrieving all the parameters at
348 the same time (Petit et al., 2017).

349 3.3. Implementation of inversion methods

350 For the six methods presented in Table 1, the cost function was iteratively optimized
351 using the trust-region reflective algorithm implemented in MATLAB[®] (version 8.0.0, The
352 MathWorks Inc., Natick, MA, 2012) within the “lsqcurvefit” function. Lower and upper op-
353 timization bounds were similar to those found in the literature for turbid waters (Hedley et al.,
354 2009; Garcia et al., 2014b, 2015), i.e., $0 \leq H \leq 30$ m, $0 \leq P \leq 0.5$ m⁻¹, $0 \leq G \leq 0.5$ m⁻¹,
355 $0 \leq X \leq 0.08$ m⁻¹, $0 \leq B_1, B_2 \leq 1.5$ and $0 \leq B \leq 1$.

356
357 A special attention was given to the initialization step. While default parameter values
358 (Lee et al., 2001; Klonowski et al., 2007; McKinna et al., 2015) or reflectance-derived values
359 (Lee et al., 1999; Dekker et al., 2011; Jay & Guillaume, 2016) may be used as initial guesses,
360 Garcia et al. (2014a,b) have shown that different initial guesses could lead to different local

361 minima and therefore different parameter estimates. This step may be more critical in the
 362 case of maximum likelihood estimation because considering spectrally-correlated noise may
 363 introduce more local minima in the parameter solution space (Garcia et al., 2014b). In this
 364 paper, we thus implemented a Latin Hypercube Sampling scheme as proposed by Garcia et al.
 365 (2014b) to generate preliminary LUTs containing 100,000 initial guesses and corresponding
 366 simulated reflectance spectra. Normal distributions were used for H , P , G and X , and uni-
 367 form distributions bounded by the above lower and upper bounds were used for B , B_1 and
 368 B_2 . Empirical values were used for means and standard deviations of normal distributions:
 369 means were set to 0, while standard deviations were set such that the value of the probability
 370 density function at half maximum corresponded to one-third of the upper bound (e.g., we
 371 used a standard deviation of 8.5 m for H). Only positive sets of parameters were then kept
 372 to build the LUTs. The use of such normal distributions allowed us to sample more finely the
 373 regions of the parameter space where the reflectance strongly varies with depth and water
 374 clarity parameters, namely, shallow waters and high water clarity (Hedley et al., 2009; Jay
 375 & Guillaume, 2016). For each measured spectrum to be inverted, the 100 sets of parameters
 376 corresponding to the 100 closest spectra in the LUT were averaged to provide a single initial
 377 guess for the iterative optimization process. In vegetation remote sensing, averaging multiple
 378 best solutions instead of retaining only the best one is known to increase the estimation
 379 accuracy when the inversion problem is ill-posed and/or the reflectance model is not fully
 380 accurate (Darvishzadeh et al., 2011; Verrelst et al., 2015; Jay et al., 2017).

381

382 In this study, four substrates were identified as possible endmembers (Fig. 4). As only
 383 two of them could be used in the bottom reflectance model (Eq. (8)), we implemented the
 384 same type of approach as Brando et al. (2009), i.e., (1) each measured reflectance spectrum
 385 was inverted using each of the six possible pairs of substrates (note that this requires gener-
 386 ating six preliminary LUTs for initialization), and (2) these six pairs were sorted according to
 387 their $P(\mathbf{r}|\Delta)$ value. For similar reasons as for initialization and unlike Brando et al. (2009)
 388 who only retained the best pair (i.e., corresponding to the highest $P(\mathbf{r}|\Delta)$ value, P_{\max}), the
 389 solution was here obtained by averaging all pairs whose $P(\mathbf{r}|\Delta)$ values were sufficiently close
 390 to P_{\max} , i.e., within $n\%$ of P_{\max} . In the following, the value of n was investigated based on

391 simulated data (Section 4.2), testing $n = 0$ (i.e., only the best pair is retained), 1 and 2%.
392 The optimum value was then used for processing the airborne data (Section 4.3).

393

394 The four bottom intra-class covariance matrices used in MILEBI and MILEBI_{S21} were
395 estimated from hyperspectral images acquired at low tide, similarly to the mean reflectance
396 spectra (see Section 2.4). It is worth noting that inverting the covariance matrices detailed in
397 Table 1 requires (at least) as many samples (i.e., spectra) as spectral bands for $\mathbf{\Gamma}_{surf}$ and $\mathbf{\Gamma}_{b,i}$
398 estimations. The more samples we have, the more accurate the estimations. In this paper,
399 a minimum of 150 spectra (for oyster bag class) were used, this number being substantially
400 higher than the number of spectral bands (35).

401 3.4. Performance assessment

402 3.4.1. Simulated data

403 We conducted two series of simulations, each of which corresponded to a different model
404 to generate the synthetic data set. For the first data set, we used the probabilistic modeling
405 of Eq. (10), therefore assuming that the random variability is only described by $\mathbf{\Gamma}_{surf}$. The
406 influence of water column properties was studied at four depths, i.e., 1, 5, 10 and 20 m, and
407 intermediate water clarity as given by Garcia et al. (2015), i.e., $P = 0.1 \text{ m}^{-1}$, $G = 0.1 \text{ m}^{-1}$,
408 and $X = 0.01 \text{ m}^{-1}$. The bottom was given either as one of the four substrates shown in
409 Fig. 4, or as a 50%/50% mixture of two substrates, thus resulting in ten tested bottom spec-
410 tra. Note that intra-class variability was not simulated for this data set. We used the $\mathbf{\Gamma}_{surf}$
411 matrix that was estimated over optically deep waters from the airborne data set presented
412 in Section 2, the diagonal of $\mathbf{\Gamma}_{surf}$ being given as the square of $\text{NE}\Delta r_E$ shown in Fig. 2. The
413 sun-sensor geometry was identical to that used for airborne acquisitions, i.e., nadir viewing
414 and a solar zenith angle of 50° .

415 The second synthetic data set was generated using the probabilistic modeling of Eq. (12).
416 As compared with the first data set, the only difference related to the simulation of bottom
417 reflectance, which was here not only modeled using multiplicative factors, but also using ran-
418 dom vectors $\mathbf{n}_{b,1}$ and $\mathbf{n}_{b,2}$. These vectors were generated based on the intra-class covariance
419 matrices estimated from airborne data (see Section 3.3).

420 For each data set, the “mvnrnd” MATLAB function allowed us to generate 100 noise-
421 perturbed spectra for every depth and bottom reflectance, hence providing 4,000 simulated
422 spectra in total. These spectra were then inverted using the six methods and according to
423 the procedure described in Section 3.3. The estimation performances were evaluated in terms
424 of mean absolute error (MAE), which has proven to be a more reliable measure of error than
425 the classical root mean square error (Willmott & Matsuura, 2005).

426 *3.4.2. Airborne data*

427 The retrievals of bathymetry, absorption of phytoplankton at 440 nm and bottom cover
428 were also assessed using the airborne data set (Section 2). For each 6×6 m² flat sandy-bottom
429 area (thus containing 12×12 pixels), the semi-analytical model was inverted for each pixel
430 using the six methods, and estimated values of H , P and bottom coefficients were compared to
431 their actual values whenever possible. The six methods were also used to retrieve the bottom
432 cover for the image presented in Fig. 3, the estimated benthic habitats being qualitatively
433 evaluated by visual inspection.

434 **4. Results and discussion**

435 *4.1. Influences of environmental noise and bottom intra-class variability on subsurface re-* 436 *flectance*

437 A preliminary study was conducted to quantify the influences of environmental noise
438 and bottom intra-class variability on the measured subsurface reflectance, based on the total
439 covariance matrix presented in Eq. (13). Representing this matrix for the four depths in-
440 vestigated in the simulations (same water quality) and the four pure substrates presented in
441 Fig. 4 allows us to see how these two sources of error make the observation deviate from the
442 model (note that, if the bio-optical model in Eq. (9) would be perfect, the total covariance
443 matrix would be the zero matrix).

444 In the absence of water, the four bottom intra-class covariance matrices show quite different
445 patterns and magnitudes (Fig. 5). While, overall, sand and oyster bag variabilities steadily
446 increase with wavelength, brown algae and, to a lesser extent, seagrasses/green algae, show
447 lower variability in the blue and red domains due to the strong chlorophyll absorption leading

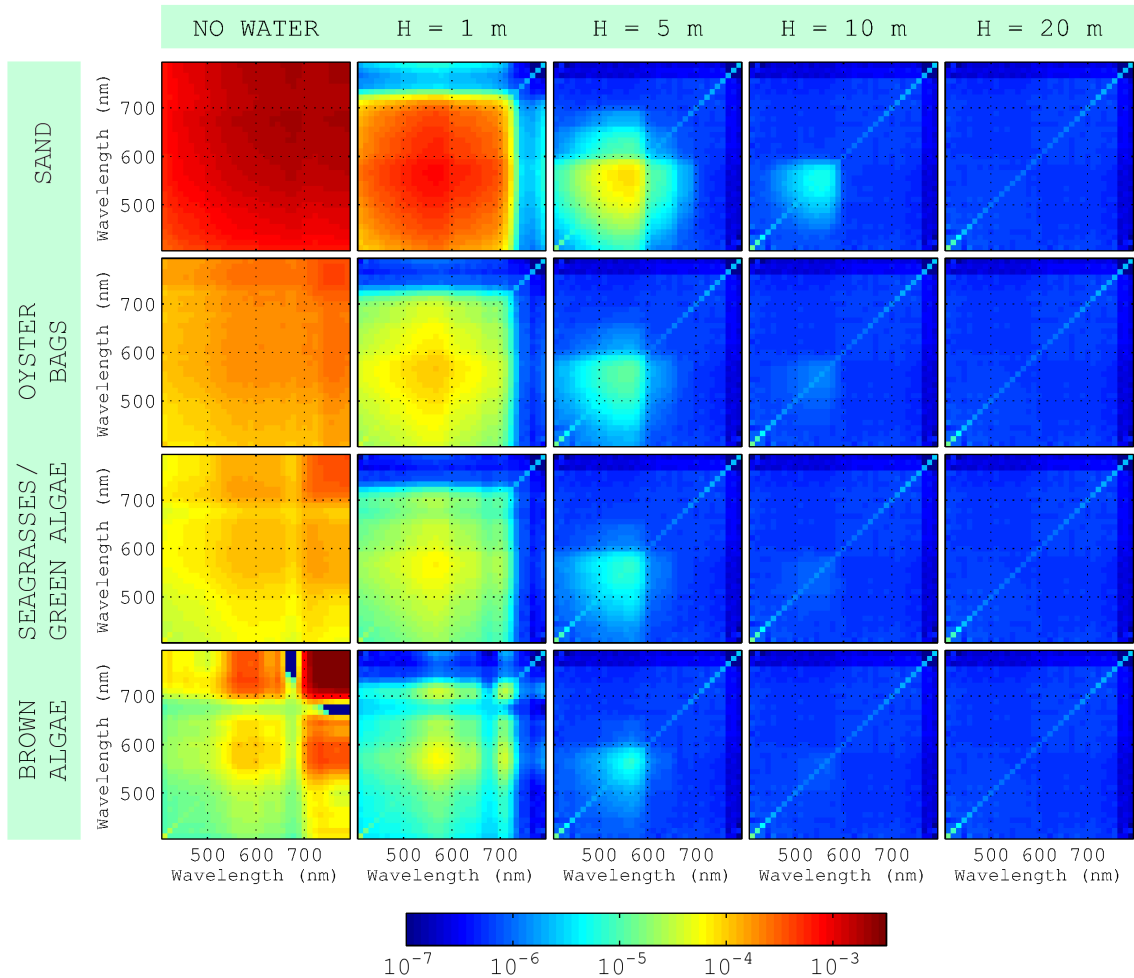


Figure 5: Total covariance matrix (as defined by Eq. (13)) as a function of depth for the four pure substrates investigated ($P = 0.1 \text{ m}^{-1}$, $G = 0.1 \text{ m}^{-1}$ and $X = 0.01 \text{ m}^{-1}$). The color scale is the same for every matrix.

448 to reflectance saturation. For the four substrates, the influence of bottom intra-class variabil-
 449 ity (resp., environmental noise) decreases (resp., increases) with increasing optical depth. At
 450 1 m and, to a lesser extent, 5 m, the subsurface reflectance variability in the visible domain is
 451 primarily driven by the bottom intra-class variability, showing that the latter should not be
 452 neglected for such optically shallow waters as also observed by Hedley et al. (2012b). Note
 453 that, at 1 m and for most wavebands larger than 700 nm, the water attenuation is already
 454 such that the total covariance matrix is mainly dominated by the environmental noise for
 455 the four substrates. At 10 m, the influence of environmental noise tends to overshadow that
 456 of bottom intra-class variability; only the variability of the brightest benthic class, namely
 457 sand, affects the subsurface reflectance in the domain of lower absorption (i.e., in the green
 458 region for this water type). In optically deep waters (20 m), the bottom is not visible so
 459 only the environmental noise contributes to the total covariance matrix. Of course, note that

460 the relative influences of environmental noise and bottom intra-class variability as functions
461 of optical depth depend on their magnitude, meaning that they should be re-evaluated for
462 every sensor, study area, etc.

463 To our knowledge, only a few authors (e.g., Hedley et al. (2012b)) have thoroughly analyzed
464 the influence of bottom intra-class spectral variability on subsurface reflectance. Using the
465 analytical expression in Eq. (13) appears as a simple but convenient way to undertake such an
466 analysis and to investigate how accurate Eq. (8) is in modeling the total bottom reflectance.

467 4.2. Estimation results obtained with the simulated data

468 In Fig. 6 and Fig. 7, we show the inversion results obtained from the two synthetic data
469 sets presented in Section 3.4.1. Importantly, as the bottom reflectance variability was simu-
470 lated differently in these two data sets, we only present LS_{S21} , $MILE_{S21}$, LS and $MILE$ (resp.
471 $MILEBI_{S21}$ and $MILEBI$) bottom estimation results when using the first (resp. the second)
472 data set. For both data sets, we, however, show the H , P , G and X estimation results for
473 the six methods in order to study the influence of bottom mismodeling.

474
475 For each method, the H estimation error is similar for both data sets and increases with
476 depth (Fig. 6). It could be shown that this increase is caused both by a progressive H un-
477 derestimation and by an increasing estimation variance. Overall, $MILE_{S21}$ and $MILEBI_{S21}$
478 (resp., $MILE$ and $MILEBI$) provide lower errors than LS_{S21} (resp., LS). For example, at 10 m
479 (first data set, $n = 0\%$), the MAEs are 1.52, 1.63 and 2.32 m for $MILEBI_{S21}$, $MILE_{S21}$ and
480 LS_{S21} resp.. Using the sum-to-one constraint generally improves the performances, especially
481 for $H \geq 5$ m, $MILEBI$, $MILE$ and LS respectively obtaining MAEs of 2.48, 2.46 and 3.14 m
482 at 10 m.

483 On the one hand, the P and G errors tend to show a bowl-shaped pattern with respect to
484 depth (the minimum being located at 5 m in most cases), especially when considering the
485 second data set. On the other hand, the X error steadily declines with increasing depth
486 (Fig. 6). Similarly to H , $MILE$ - and $MILEBI$ -based methods generally better estimate these
487 water clarity parameters than LS -based methods. This is more visible for $H \geq 5$ m, for
488 which similar errors are generally obtained with $MILE_{S21}$, $MILEBI_{S21}$, $MILE$ and $MILEBI$.

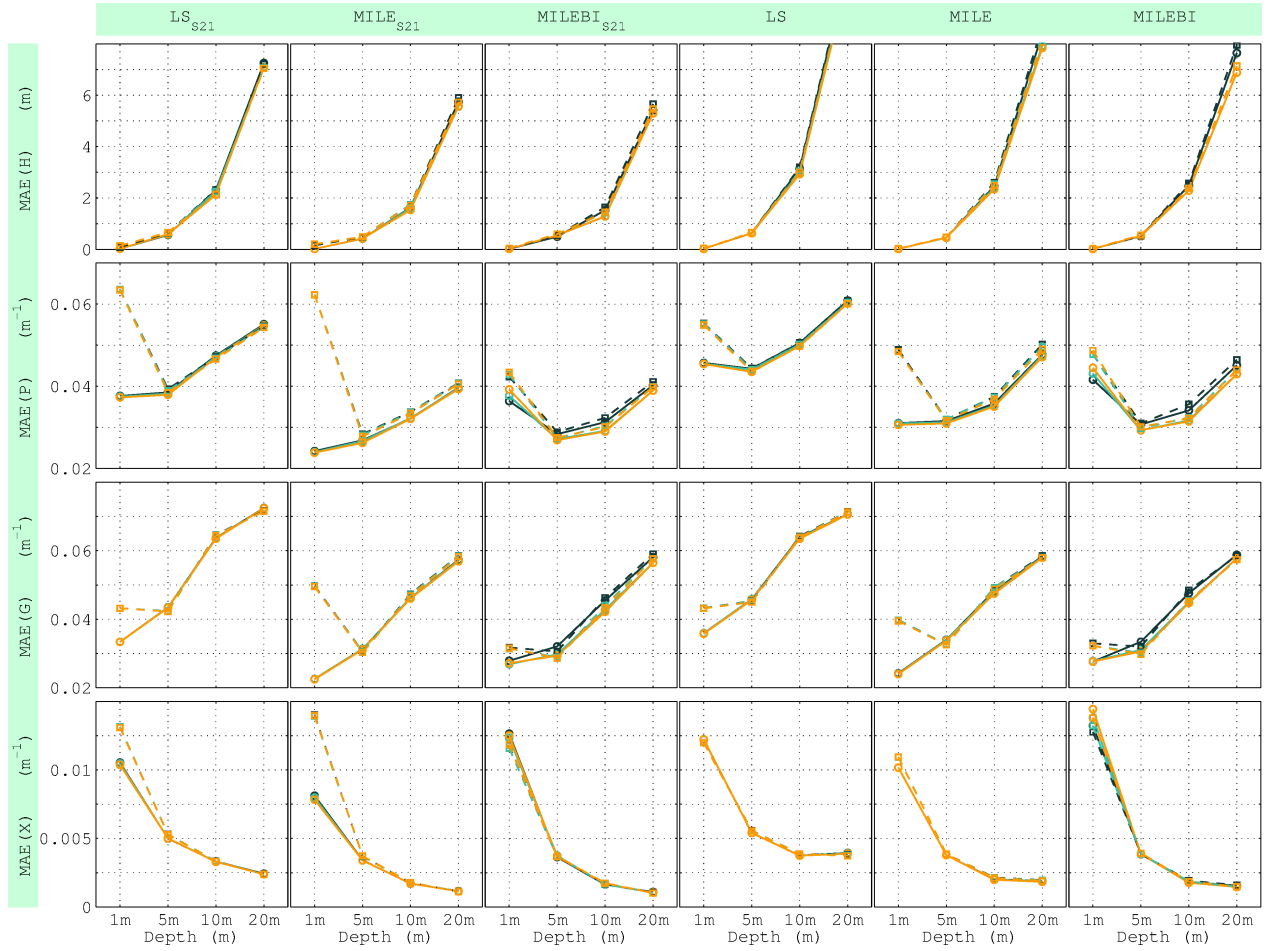


Figure 6: H , P , G and X (rows 1-4, resp.) estimation results obtained by applying the six methods (columns 1-6, resp.) presented in Table 1 to the synthetic data simulated using either Eq. (10) (solid lines) or Eq. (12) (dashed lines). Black, turquoise and orange lines respectively correspond to the use of $n = 0, 1$ and 2% for averaging the best bottom pairs.

489 For example, at 10 m (first data set, $n = 0\%$), the P (resp., X) retrieval error decreases by
 490 about 30% (resp., 48%) when using one of these four methods instead of LS_{S21} or LS .

491 While both data sets lead to similar results for $H \geq 5$ m, strong differences appear for
 492 $H = 1$ m. When using the first data set, MILE-based methods offer the best performances
 493 for P and G , followed by MILEBI- and LS -based methods. In the case of X , MILE_{S21} and
 494 MILE still perform better, followed by LS - and MILEBI-based methods. However, the errors
 495 obtained with MILE- and LS -based methods increase when using the second data set. This
 496 increase is stronger (1) when the bottom mixture coefficients are constrained to sum to one
 497 (e.g., for P estimation, the MAEs obtained with LS_{S21} and LS increase by 70 and 21% resp.),
 498 and (2) in the cases of MILE-based methods as compared to LS -based methods (e.g., for
 499 X estimation, the MAEs obtained with LS_{S21} and MILE_{S21} increase by 26 and 78% resp.).

500 On the other hand, MILEBI-based methods offer more similar results over both data sets,
501 MILEBI_{S21} generally performing better than the other methods for these three parameters
502 when using the second data set.

503 Using $n = 0, 1$ or 2% for averaging the best bottom pairs does not significantly change the
504 H, P, G and X inversion results for LS- and MILE-based methods. For MILEBI_{S21} and
505 MILEBI, increasing the value of n generally slightly degrades the estimation accuracy at 1 m
506 (e.g., for P estimation, the MAE obtained with MILEBI_{S21} increases by 7% when taking
507 $n = 2\%$ as compared to $n = 0\%$). However, the performances generally improve for $H \geq 5$ m
508 when taking either $n = 1$ or 2% . For example, at 10 m (first data set) and for both n values,
509 the MAE obtained with MILEBI_{S21} decreases by 15% for H and 7% for P .

510

511 The bottom estimation results show similar trends for every benthic class, method, data
512 set and n value, i.e., the error increases with depth (Fig. 7). For $H \leq 5$ m, the easiest
513 class to be retrieved is generally sand, followed by brown algae, seagrasses/green algae and
514 oyster bags. For deeper waters, it is more difficult to note any clear trend among methods
515 and benthic classes. Similarly to depth and water clarity parameters, MILE-based methods
516 provide equal or better performances than LS-based methods for $H \leq 5$ m (e.g., for the sand
517 coefficient, the MAEs obtained with LS_{S21} and MILE_{S21} at 5 m are 0.13 and 0.09 resp.).
518 It is worth noting that, despite the additional bottom intra-class variability present in the
519 second data set, the performances of MILEBI-based methods generally remain comparable to
520 those of MILE-based methods. Also, it can be seen that applying the sum-to-one constraint
521 significantly improves the retrieval for every method, especially for $H \geq 5$ m. For example,
522 for the oyster bag coefficient, the MAE obtained with MILEBI_{S21} at 5 m ($n = 0\%$) increases
523 by 38% when relaxing the sum-to-one constraint.

524 Averaging over several bottom pairs instead of retaining only the best one generally has a
525 positive effect for every method and $H \geq 10$ m (or even for $H \geq 5$ m in the cases of LS
526 and MILE). For such optically deep waters, taking $n = 2\%$ and, to a lesser extent, $n = 1\%$,
527 provides equal or better performances than taking $n = 0\%$ in most cases. For example, for
528 the sand coefficient, the MAE obtained with LS_{S21} at 10 m decreases by 13% when taking
529 $n = 2\%$ as compared to $n = 0\%$. For shallower waters, this averaging does not significantly

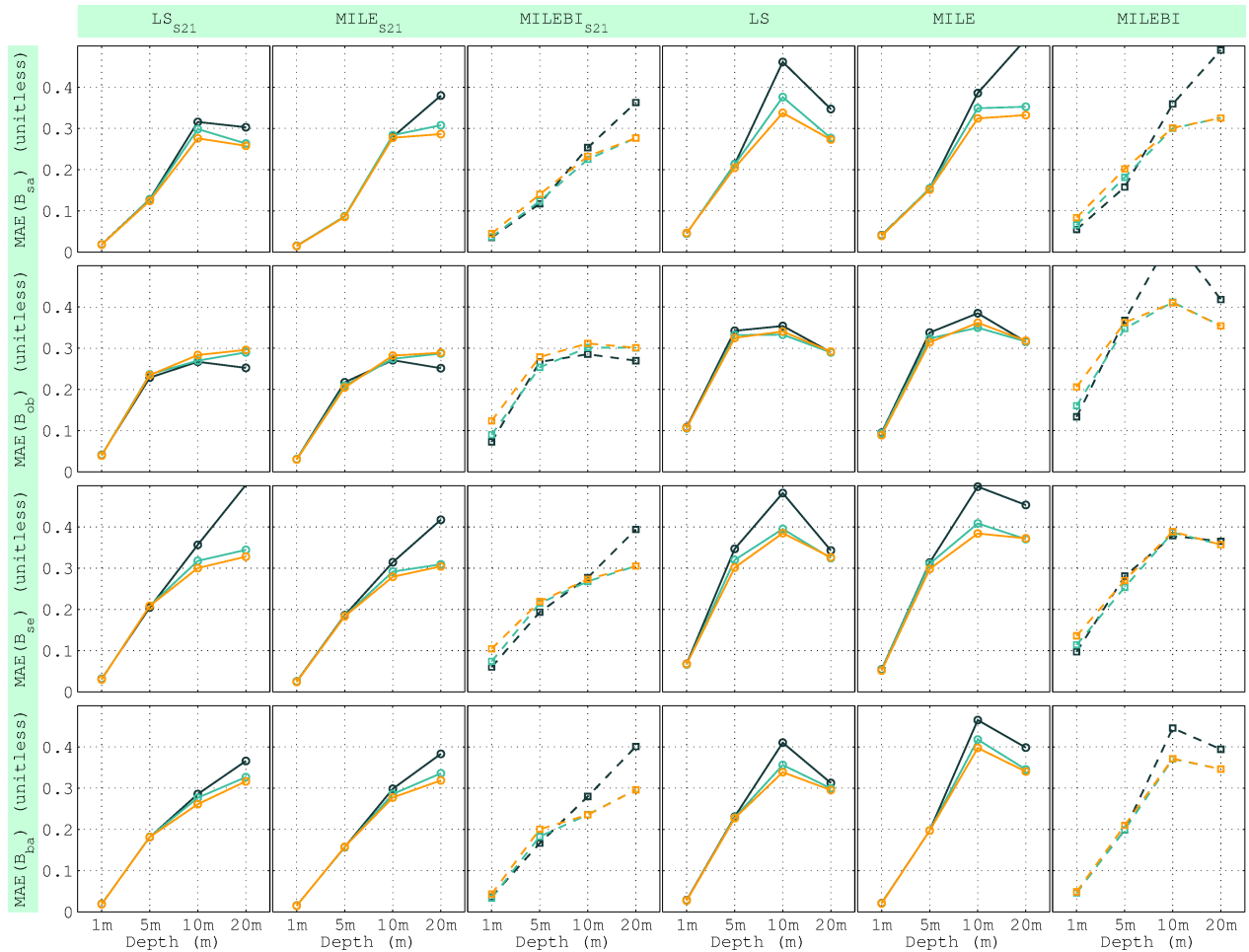


Figure 7: Bottom estimation results obtained by applying the six methods (columns 1-6, resp.) presented in Table 1 to the synthetic data simulated using either Eq. (10) (solid lines) or Eq. (12) (dashed lines). Black, turquoise and orange lines respectively correspond to the use of $n = 0, 1$ and 2% for averaging the best bottom pairs. B_{sa} , B_{ob} , B_{se} and B_{ba} (rows 1-4, resp.) refer to the coefficients of sand, oyster bag, seagrass/green alga and brown alga spectra, resp..

530 change the retrieval accuracy for LS- and MILE-based methods. However, taking $n = 2\%$,
 531 and, to a lesser extent, $n = 1\%$, slightly degrades the MILEBI_{S21} and MILEBI bottom
 532 estimation results. In the following results, n is therefore set to 1% as this value offers a good
 533 compromise between optically shallow and deep waters for the six methods.

534 4.3. Estimation results obtained with the airborne data

535 Similarly to simulations, for every method, the H estimation error increases with depth
 536 as a result of a progressive H underestimation and an increasing estimation variance (Fig. 8).
 537 This underestimation occurs for shallower waters in the cases of LS-based methods as com-
 538 pared to MILE- and MILEBI-based methods. Unlike for simulations, the sum-to-one con-
 539 straint leads to poorer performances for every method. MILEBI provides the highest overall

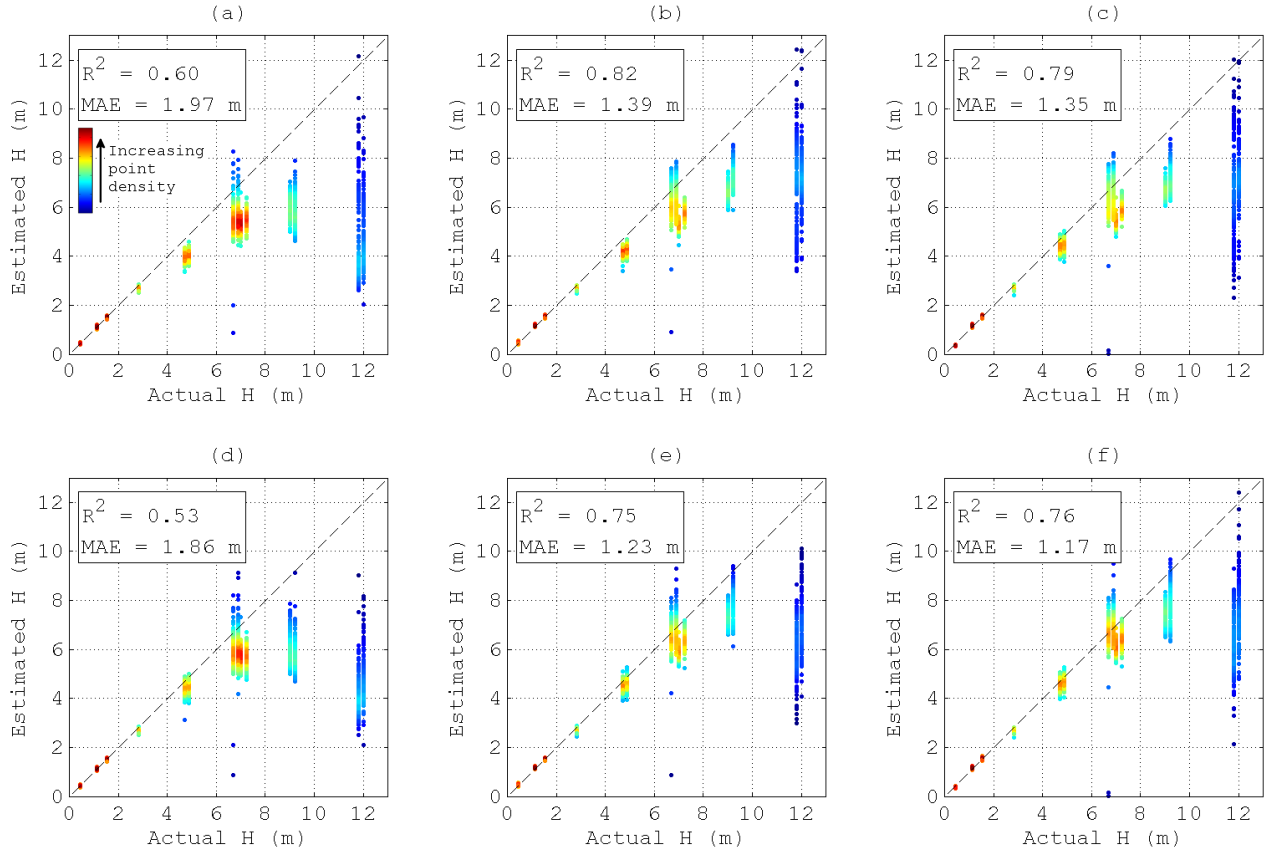


Figure 8: Depth estimation results obtained from airborne data ($n = 1\%$): (a) LS_{S21} , (b) $MILE_{S21}$, (c) $MILEBI_{S21}$, (d) LS , (e) $MILE$ and (f) $MILEBI$.

540 accuracy (MAE = 1.17 m), followed by MILE (MAE = 1.23 m), $MILEBI_{S21}$ (MAE = 1.35 m)
 541 and $MILE_{S21}$ (MAE = 1.39 m). On the other hand, LS_{S21} and LS obtain significantly higher
 542 errors, with MAEs of 1.97 and 1.86 m respectively. Note that Fig. 8 suggests that the water
 543 tends to be quasi-optically deep for $H > 10$ m, thus potentially making the comparison mis-
 544 leading. When removing the samples corresponding to $H > 10$ m, the MAEs become 0.49,
 545 0.53, 0.75 and 0.81 m for $MILEBI$, $MILE$, $MILEBI_{S21}$ and $MILE_{S21}$, respectively. On the
 546 other hand, LS and LS_{S21} still obtain poorer performances, with MAEs of 0.92 and 1.12 m,
 547 respectively. These MAEs are about twice as high as those obtained using $MILEBI$ and $MILE$.

548

549 Similar observations are made from the P inversion results (Fig. 9), i.e., (1) $MILE$ - and
 550 $MILEBI$ -based methods perform better than LS -methods, and (2) relaxing the sum-to-one
 551 constraint improves the estimation accuracy. $MILEBI$ and $MILE$ still provide the best per-
 552 formances with $MAE \approx 0.016 \text{ m}^{-1}$, while LS_{S21} and LS lead to $MAE \approx 0.027 \text{ m}^{-1}$.

553

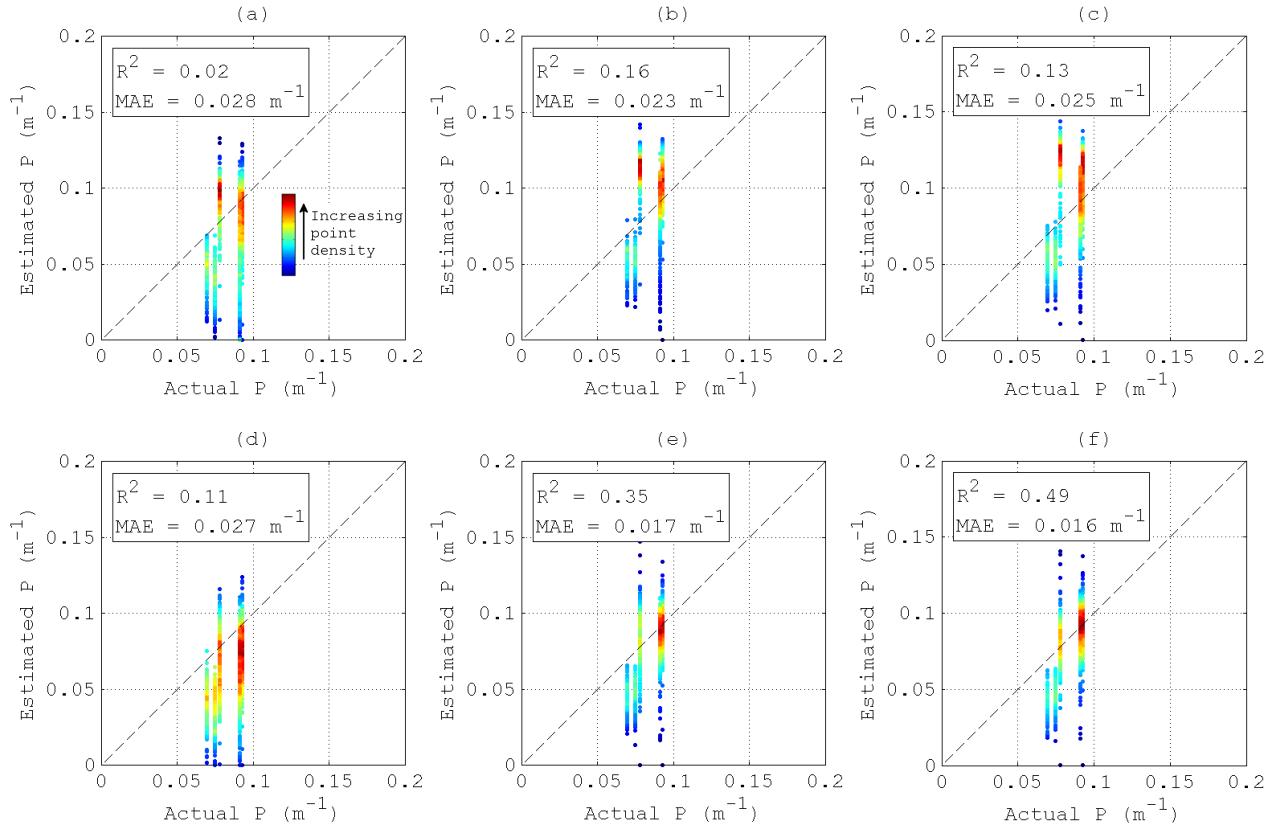


Figure 9: P estimation results obtained from airborne data ($n = 1\%$): (a) LS_{S21}, (b) MILE_{S21}, (c) MILEBI_{S21}, (d) LS, (e) MILE and (f) MILEBI.

554 The bottom estimation results obtained from the 14 areas of known depth (Fig. 10) show
 555 the same pattern for every method, i.e., (1) the sandy-bottom cover is accurately retrieved
 556 in shallow waters, and (2) the estimated sand coefficient decreases as depth increases, which
 557 is compensated for by increasing coefficients of darker substrates. This decrease occurs for
 558 shallower waters (i.e., for $H \geq 4.70$ m) for the three methods that do not constrain the sum
 559 to one, i.e., LS, MILE and MILEBI. For example, for these methods and $H \geq 4.70$ m, the
 560 estimated sand coefficient generally does not exceed 0.5, while the estimated brown alga co-
 561 efficient is mostly close to 1.5. On the other hand, LS_{S21}, MILE_{S21} and MILEBI_{S21} generally
 562 lead to reasonable estimates of bottom cover until around 9.00 m, the best performances
 563 being obtained using MILE_{S21} with a minimum estimated sand coefficient of 0.6.

564

565 In Fig. 11, the same concise and qualitative RGB representation as Petit et al. (2017) is
 566 adopted to show the estimated spatial distributions of the four investigated substrates based
 567 on the image presented in Fig. 3. Beforehand, for each pixel, the four estimated bottom

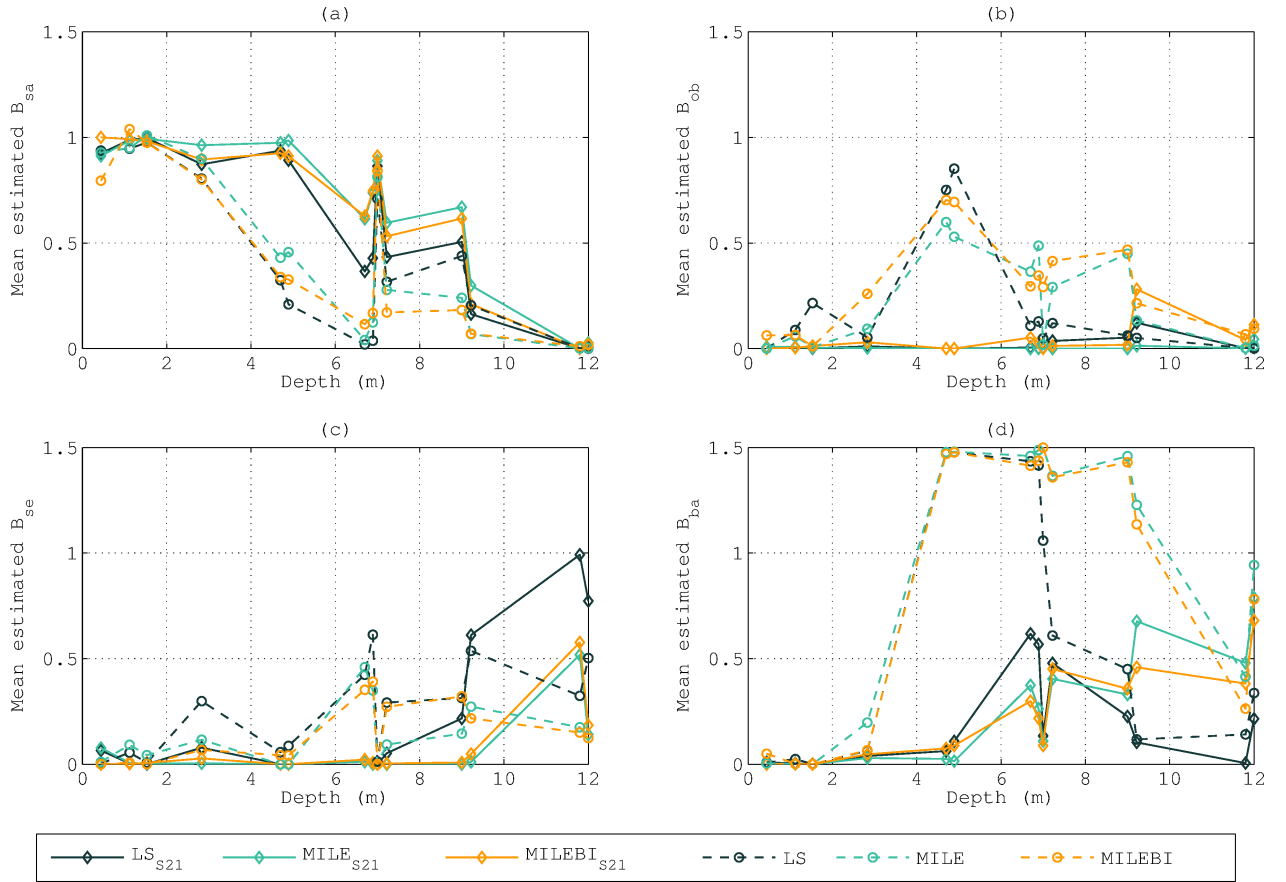


Figure 10: Mean estimated coefficients for (a) sand (B_{sa}), (b) oyster bags (B_{ob}), (c) seagrasses/green algae (B_{se}) and (d) brown algae (B_{ba}) for the 14 sandy-bottom areas ($n = 1\%$).

568 coefficients were normalized by their sum (that obviously equals one for LS_{S21} , $MILE_{S21}$ and
569 $MILEBI_{S21}$) so that the obtained normalized coefficients were closer to the actual fractional
570 covers (if we assume that the effect of intra-class variability is lower than that of fractional
571 cover), which facilitates the comparison of the six methods. This allows representing (1) the
572 distributions of oyster bags, seagrasses/green algae and brown algae through the blue, green
573 and red channels of the color composite image, resp., and (2) the distribution of sand through
574 the absence of blue, green and red, i.e., through the pixel darkness.

575 The large sandy-bottom area is accurately retrieved by LS_{S21} , $MILE_{S21}$ and $MILEBI_{S21}$, the
576 LS_{S21} map being slightly noisier than the other two, e.g., in the deeper (upper right) part
577 of the image. Except in the shallower (left-hand) part of the image for $MILEBI$, relaxing
578 the sum-to-one constraint leads to poorer results in the main sandy area. Indeed, even
579 if LS , $MILE$ and $MILEBI$ retrieve some sand, they greatly overestimate the presence of
580 seagrasses/green algae, brown algae and oyster bags respectively.

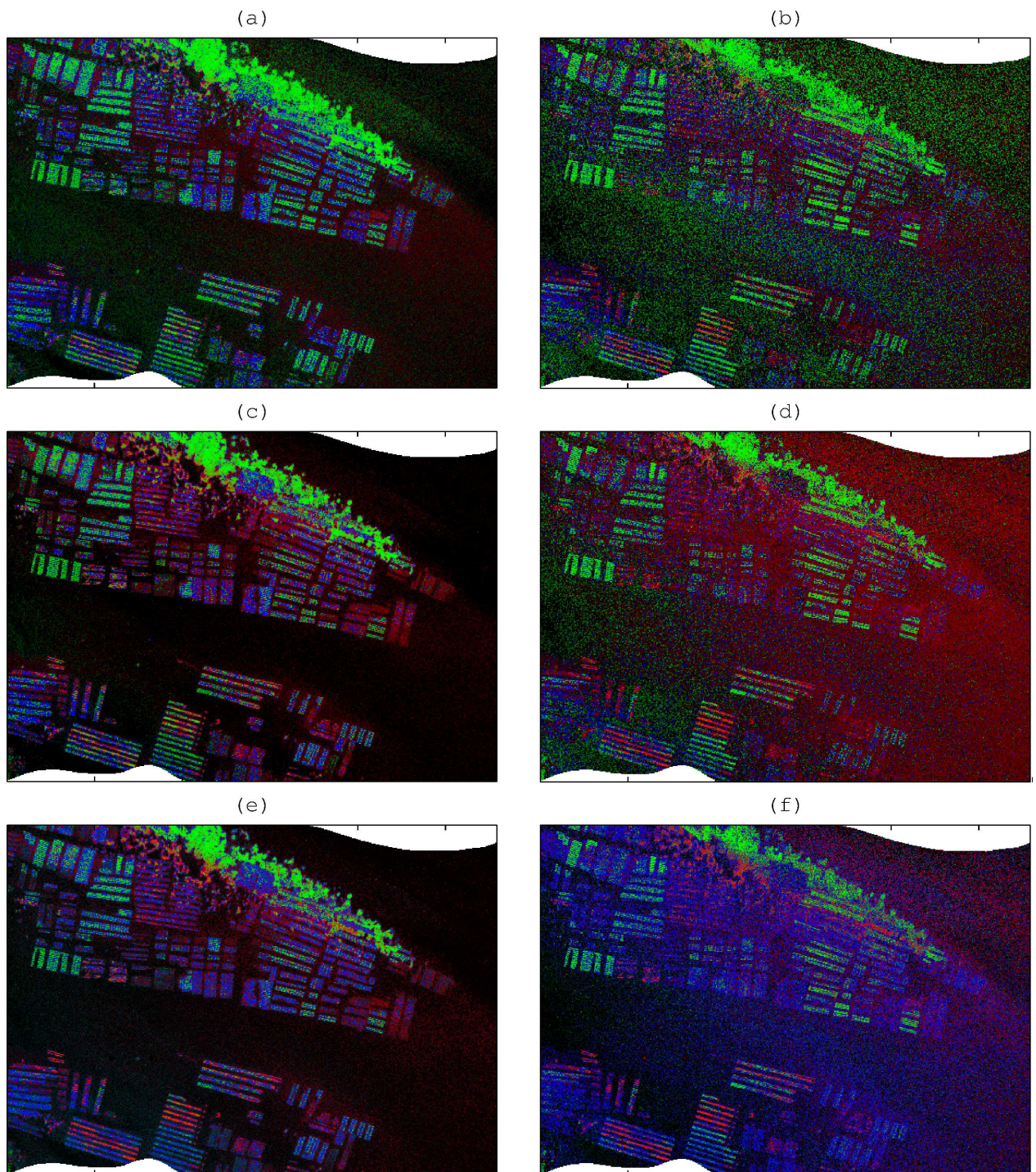


Figure 11: Color composite images showing the estimated spatial distributions of the four investigated substrates based on the image presented in Fig. 3: (a) LS_{S21} , (b) LS , (c) $MILE_{S21}$, (d) $MILE$, (e) $MILEBI_{S21}$, and (f) $MILEBI$ ($n = 1\%$). The normalized estimated coefficients of oyster bags, seagrasses/green algae and brown algae are respectively coded by the blue, green and red channels. The normalized estimated sand coefficient is coded by the pixel darkness (i.e., the absence of red, green and blue).

581 Overall, the six methods accurately retrieve the seagrass meadow. Some confusions with
582 brown algae however occur in the lower and shallower part of the meadow when using MILE,
583 MILEBI, and to a lesser extent, MILEBI_{S21}, MILE_{S21} and LS_{S21}.

584 Similarly to what is observed with simulations, the retrieval of oyster bag distribution is
585 generally less accurate. The results are seemingly more consistent with MILEBI_{S21} and
586 MILEBI, as both methods obtain higher and more homogeneously-distributed oyster bag
587 coefficients over oyster racks as compared to the other methods. Note that only the MILE_{S21}
588 and MILEBI-based methods can reliably detect the deepest oyster racks located within the
589 seagrass meadow. On the other hand, LS_{S21} obtains a spatially-inconsistent mixture of oyster
590 bags and seagrasses, while LS and MILE retrieve a sand-dominated bottom.

591 It is worth noting that the brown algae retrieved by MILEBI_{S21} over some oyster racks in the
592 lower left part of the image are more sparsely detected by MILE_{S21} and almost not detected
593 by LS_{S21}. These brown algae are, however, consistently retrieved by the three methods with
594 relaxed sum-to-one constraint.

595 *4.4. Discussion of estimation performances*

596 *4.4.1. General considerations*

597 By definition, a bio-optical model is only a model, which means that various sources of
598 error may make it deviate from the observation. Given the number of potential sources (e.g.,
599 environmental noise or bottom intra-class variability), the difficulty to properly take them
600 into account (e.g., skyglint) and the low water-leaving radiance, it seems quite challenging
601 to include them explicitly within the modeling and to estimate the corresponding additional
602 parameters during the inversion process. Yet, the results presented in Fig. 5 show that
603 such variability may make the shallow water reflectance strongly differ from the bio-optical
604 model. As a result, it may significantly decrease the estimation accuracy as obtained using the
605 classical LS method, since the latter tries to perfectly match the model with the observation.
606 Alternatively, we propose to include these deviations within a probabilistic forward model of
607 shallow water reflectance variability, thus assuming that they all can be described through
608 an additive zero-mean multivariate Gaussian noise that is fully determined by its spectral
609 covariance matrix. The MILE- and MILEBI-based inversion methods are derived from such

610 probabilistic modeling, and the results derived from simulated and airborne data show that
611 they all succeed in decreasing the detrimental influence of environmental noise as compared to
612 LS-based methods, especially in optically deep waters. In addition, MILEBI-based methods
613 decrease the influence of bottom intra-class variability, especially in very optically shallow
614 waters.

615 *4.4.2. Common trends in method performances*

616 Overall, the results obtained with simulated and airborne data show similar trends and
617 are consistent with expectations for every method. For example, depth and benthic cover
618 estimations become less accurate as depth increases due to the decreasing bottom influence
619 on subsurface reflectance (Fig. 6, Fig. 7, Fig. 8 and Fig. 10). The retrievals of water clarity
620 parameters differ between absorbing (P and G) and scattering (X) components that respec-
621 tively decrease and increase the subsurface reflectance (Fig. 6). For P and G , the depth
622 of minimum error is the one that offers the best compromise between (1) maximizing the
623 subsurface reflectance so that there is more contrast between absorbing and non-absorbing
624 regions (which facilitates the retrieval), and (2) minimizing the influence of bottom variabil-
625 ity on subsurface reflectance. For X , the error is minimum in optically deep waters, where
626 the bottom does not affect the subsurface reflectance.

627 *4.4.3. Influence of averaging the best bottom pairs*

628 Due to the ill-posedness of the inversion problem (resulting in compensations between
629 model parameters) or to potential deviations between the measured reflectance and the
630 model, the actual bottom pair may not be the one that leads to the lowest cost function
631 value. In simulations, the inversion is particularly ill-posed for quasi-optically deep waters,
632 where (1) H and coefficients of dark bottoms often tend to compensate, and (2) all the dark
633 benthic classes (e.g., seagrasses/green algae and brown algae) nearly have the same effect on
634 subsurface reflectance (Fig. 6 and Fig. 7). In this case, selecting a particular dark substrate
635 in the bottom spectral library instead of another dark substrate is not strongly justified,
636 given the different sources of error between the observed and modeled reflectances that ac-
637 tually make both substrates equally likely. The results (Fig. 6 and Fig. 7) demonstrate that,
638 alternatively, taking the average of multiple best bottom pairs (if sufficiently close to the

best pair) can decrease the ill-posedness influence and increase the overall retrieval accuracy, acting as a regularization step. Testing the effect of the n value (that directly controls the number of best pairs to be averaged), we show that a high n value (even greater than 2%) can be chosen for optically deep waters, where a reasonable aim is only to discriminate among bright and dark substrates. In very shallow waters, a too large n value may, however, increase the confusion between classes, therefore making the value of 1% a good compromise for our data. Of course, this value should be reassessed for each data set, as it is expected to depend on, e.g., the environmental noise and/or the benthic classes encountered on the study site.

4.4.4. Influence of sum-to-one constraint

The results show that the sum-to-one constraint always leads to better inversion results if the shallow water reflectance model is perfect (e.g., when applying LS- and MILE-based methods to the first data set, or MILEBI-based methods to the second data set), because reducing the number of parameters to be retrieved reduces the estimation uncertainty. In practice, the observation may, however, deviate from the model. These deviations may be caused either by the observation, e.g., in the case of imperfect preprocessing of at-sensor radiance (e.g., atmospheric and sea surface corrections), or by the model, e.g., in the case of imperfect bio-optical modeling. In this study, such deviations are present when considering airborne remote-sensing data or when applying LS- and MILE-based (resp., MILEBI-based) methods to the second (resp., first) synthetic data set. In these cases, relaxing the sum-to-one constraint adds a degree of freedom, which enables unmodeled (or mismodeled) variability to be compensated for by misestimation of bottom cover rather than by misestimation of depth and/or water clarity parameters. This is demonstrated by the results obtained with airborne data, since (1) Fig. 8 and Fig. 9 show that LS, MILE and MILEBI better retrieve H and P as compared to LS_{S21} , $MILE_{S21}$ and $MILEBI_{S21}$ resp. (note that this is consistent with the results of Petit et al. (2017) in the case of LS), and (2) Fig. 10 shows that LS_{S21} , $MILE_{S21}$ and $MILEBI_{S21}$ provide better bottom retrievals than LS, MILE and MILEBI resp.. However, relaxing the sum-to-one constraint does not always degrade the bottom retrieval: indeed, if the bottom intra-class variabilities affect the subsurface reflectance (i.e., mostly for low optical depths, see Fig. 5), allowing both benthic reflectances in Eq. (8) to vary in

668 a multiplicative way enables LS and MILE to better capture this intra-class variability and
669 improve the overall performances.

670 MILEBI_{S21} thus appears as an interesting alternative to LS- and MILE-based methods, be-
671 cause (1) it takes into account potentially complex (i.e., not only multiplicative) bottom
672 intra-class variabilities through their associated covariance matrix, and (2) it limits the prob-
673 lem ill-posedness as it does not require any additional parameter to be estimated. The benthic
674 covers derived from airborne data (Fig. 11) illustrate this dual improvement, as MILEBI_{S21}
675 not only provides accurate performances in the deepest sandy-bottom areas similarly to LS_{S21}
676 and MILE_{S21}, but also retrieves the presence of brown algae over oyster racks in shallower
677 waters, similarly to LS, MILE and MILEBI.

678 4.4.5. *Robustness of inversion methods*

679 All LS-, MILE- and MILEBI-based methods require some prior knowledge on the con-
680 sidered scene, this knowledge concerning either the mean endmember reflectances or the
681 covariance matrices. However, obtaining an accurate prior knowledge may be difficult, which
682 requires investigating how such errors can affect the method performances.

683 It should first be noted that obtaining an accurate estimate of the environmental noise ma-
684 trix (as necessary for MILE- and MILEBI-based methods) is usually not problematic, since
685 it only necessitates finding a homogeneous area in the image. This may easily be done using
686 the methodology proposed by Wettle et al. (2004), and areas of optically deep water are ideal
687 to perform this estimation. Using this matrix for inversion allows MILE-based methods to
688 greatly improve the retrieval of depth and water clarity parameters in sufficiently deep waters
689 as compared to LS-based methods (Fig. 6, Fig. 8 and Fig. 9). It also improves the remote
690 sensing of shallow waters if Eq. (8) accurately models the actual bottom reflectance. How-
691 ever, if the latter cannot accurately be modeled by Eq. (8) (e.g., due to complex intra-class
692 variabilities or poorly-known mean endmember reflectances) while having a strong effect on
693 subsurface reflectance (i.e., in very optically shallow waters), the performances of MILE-
694 based methods may decrease more strongly than those of LS-based methods (Fig. 6). In
695 such cases, MILE is shown to better estimate depth and water clarity parameters than LS,
696 LS_{S21} and MILE_{S21} (Fig. 6, Fig. 8 and Fig. 9), especially because relaxing the sum-to-one

697 constraint reduces the detrimental influence of bottom intra-class variability.
698 Alternatively, MILEBI and MILEBI_{S21} allow the modeled endmember spectra to vary around
699 their mean through the use of bottom intra-class covariance matrices. Both methods are thus
700 less affected by an imperfect knowledge of endmember reflectances. This aspect is one of the
701 primary advantages of these methods as compared to LS- and MILE-based methods, and
702 may be of tremendous importance when mapping poorly-known shallow water environments,
703 for which the use of a single mean reflectance spectrum for each benthic class may seem
704 unrealistic.

705 However, obtaining accurate estimates of bottom covariance matrices may sometimes be diffi-
706 cult since, similarly to the mean endmember reflectances used by the six tested methods, and
707 as emphasized in Section 2.4, these matrices are estimated from a limited number of spectra
708 that may not be fully representative of the variability encountered in the whole study area.
709 That said, the results obtained with simulated data (Fig. 6) suggest that accurate knowl-
710 edge of these matrices may only be necessary for very optically shallow waters, as MILE- and
711 MILEBI-based obtain nearly the same results over both data sets beyond 5 m. As the optical
712 depth increases, the water attenuation and environmental noise smooths the spectral details
713 present in bottom covariance matrices (Fig. 5), so rough estimates become sufficient to take
714 this variability into account. For very optically shallow waters, unlike LS- and MILE-based
715 methods, MILEBI-based methods show similar performances for both synthetic data sets
716 (Fig. 6), although the first data set is generated using zero covariance matrices that strongly
717 differ from those used in MILEBI_{S21} and MILEBI. This important result demonstrates the
718 robustness of these two methods against imperfect knowledge of bottom covariance matrices,
719 which may have important implications for their implementation at larger scales (e.g., global
720 scale).

721 5. Conclusions and perspectives

722 In this study, we propose a realistic probabilistic model of shallow water reflectance vari-
723 ability as well as two associated inversion methods, denoted MILE and MILEBI. As compared
724 to classical least-squares fitting, these methods improve the remote sensing of shallow waters
725 by utilizing specific parameterizations of the spectral covariance matrix. MILE and MILEBI

726 not only constrain model inversion based on the off-diagonal terms of covariance matrices, but
727 also allow the measured data to differ from the model by giving the less reliable wavebands
728 lower weights in the cost function. For MILE, these wavebands correspond to the domains
729 where the environmental noise is the strongest. For MILEBI, the less reliable wavebands
730 not only correspond to the domains of strong environmental noise, but also to the domains
731 where the bottom intra-class variability is the highest. To our knowledge, MILEBI is one of
732 the first shallow water remote-sensing methods that explicitly take into account the inherent
733 variability of each benthic class without adding any multiplicative parameter to be estimated
734 during the inversion process (the bottom covariance matrices, however, need to be estimated
735 beforehand, similarly to the mean endmember reflectances).

736 Based on simulated and airborne data, we show that these specific covariance parameteriza-
737 tions enable MILE and MILEBI to generally perform better than LS. Further, studying the
738 influence of constraining bottom mixture coefficients to sum to one shows that this constraint
739 provides better inversion results if the reflectance model reliably describes the observation. In
740 the presence of unmodeled (or mismodeled) variability in the remote-sensing data (e.g., due to
741 bottom intra-class variability, imperfect atmospheric correction or bio-optical modeling, etc),
742 relaxing this constraint may decrease the detrimental influences of these deviations, however
743 at the cost of an increasingly noisy bottom retrieval as the optical depth increases. In prac-
744 tice, as there are always some slight deviations between measured and simulated data, these
745 results thus suggest that most inversion methods cannot accurately retrieve all the targeted
746 parameters at the same time, and that applying different constraints during the inversion
747 will lead these deviations to affect the estimation of other unconstrained parameters. That
748 said, the sum-to-one constrained version of MILEBI combines the advantage of limiting the
749 number of parameters to be estimated (thus reducing the problem ill-posedness) with that
750 of allowing the observation to differ from the model. This dual aspect makes this method
751 promising to remotely sense complex shallow water environments.

752

753 Future studies would certainly benefit from the probabilistic forward model of shallow
754 water reflectance variability presented in Eq. (12) so as to generate more realistic data sets
755 than those usually generated using Eq. (10). This model could also be combined with other

756 bottom reflectance models (e.g., a single substrate model, linear models including more than
757 two substrates or even non-linear mixing models) in order to further refine the modeling of
758 bottom reflectance and improve the inversion performances. This may be important for more
759 accurately simulating the response of very shallow waters, for which an increase in bottom
760 modeling complexity significantly affects the measured subsurface reflectance.

761 As far as the inversion is concerned, perspectives include refining the initialization part, that
762 may be critical for MILE methods in very shallow waters (results not shown). Optimizing the
763 construction of the LUT used for initialization (size, parameter distributions, etc) is likely
764 to speed up the inversion while keeping similar estimation performances. Alternatively, the
765 Mahalanobis distance used in MILE could easily be used as a metric within a LUT-based
766 inversion approach such as ALLUT (Hedley et al., 2009) in order to further speed up the
767 inversion process or to avoid local minima. Note that the approach recently proposed by Jay
768 & Guillaume (2016) could also be implemented to regularize the inversion by introducing
769 prior knowledge on targeted parameters.

770 Ultimately, an important perspective is the assessment of MILE and MILEBI performances
771 for shallow water remote sensing at the global scale, e.g., in the context of the forthcoming
772 “Environmental Mapping and Analysis Program” mission (Guanter et al., 2015). For this
773 purpose, besides properly estimating the environmental noise on the image itself, a generic
774 library of bottom mean reflectance spectra will be necessary to parameterize the total benthic
775 reflectance. This library may be built from a comprehensive spectral database gathering all
776 the expected bottom classes in the considered study site. For example, the 12-class database
777 presented by Hochberg et al. (2003) could be of great help for coral reef remote sensing. This
778 database could also be used to build an associated generic library of intra-class covariance
779 matrices to implement MILEBI. As shown by Hochberg et al. (2003) in Fig. 3, the intra-
780 class variability at the global scale is such that using a single mean reflectance spectrum
781 for each bottom class to map this class across different areas worldwide seems to be highly
782 unrealistic. MILEBI thus offers an interesting alternative to LS and MILE to take such
783 variability into account in a more accurate manner. In particular, given the high intra-class
784 variabilities presented by Hochberg et al. (2003) and the significant overlaps between these
785 classes, MILEBI may greatly improve the remote sensing of coral reefs.

786 Acknowledgments

787 This work was supported by the French Defense Procurement Agency (DGA) with the
788 reference ANR-15-ASTR-0019 (HypFoM). We are also grateful to Actimar, that carried out
789 the field measurement campaign (Smet et al., 2010) within the exploratory research and
790 innovation project “HypLitt”, funded by the French Defence Agency (DGA). ActiMar was
791 a company based in Brest, France, and specialized in operational oceanography and high-
792 resolution remote sensing (www.actimar.fr). These activities are now carried out by the
793 Hytech Imaging company (www.hytech-imaging.fr). Many thanks to Marc Lennon, John D.
794 Hedley and the anonymous reviewers for their valuable comments. Note, finally, that the
795 codes of the proposed methods are available on demand.

796 References

- 797 AFNOR (December 1999). *Qualité de l'eau, Dosage de la chlorophylle a et d'un indice*
798 *phopigments - Méthode par spectrométrie d'absorption moléculaire.*
- 799 Albert, A., & Gege, P. (2006). Inversion of irradiance and remote sensing reflectance in
800 shallow water between 400 and 800 nm for calculations of water and bottom properties.
801 *Applied Optics*, 45, 2331–2343.
- 802 Albert, A., & Mobley, C. (2003). An analytical model for subsurface irradiance and remote
803 sensing reflectance in deep and shallow case-2 waters. *Optics Express*, 11, 2873–2890.
- 804 Andréfouët, S., Berkelmans, R., Odriozola, L., Done, T., Oliver, J., & Müller-Karger, F.
805 (2002). Choosing the appropriate spatial resolution for monitoring coral bleaching events
806 using remote sensing. *Coral Reefs*, 21, 147–154.
- 807 Aschbacher, J., & Milagro-Pérez, M. P. (2012). The European Earth monitoring (GMES)
808 programme: Status and perspectives. *Remote Sensing of Environment*, 120, 3–8.
- 809 Botha, E. J., Brando, V. E., Anstee, J. M., Dekker, A. G., & Sagar, S. (2013). Increased spec-
810 tral resolution enhances coral detection under varying water conditions. *Remote Sensing*
811 *of Environment*, 131, 247–261.

- 812 Brando, V., Anstee, J., Wettle, M., Dekker, A., Phinn, S., & Roelfsema, C. (2009). A physics
813 based retrieval and quality assessment of bathymetry from suboptimal hyperspectral data.
814 *Remote Sensing of Environment*, *113*, 755–770.
- 815 Brando, V. E., & Dekker, A. G. (2003). Satellite hyperspectral remote sensing for estimating
816 estuarine and coastal water quality. *Geoscience and Remote Sensing, IEEE Transactions*
817 *on*, *41*, 1378–1387.
- 818 Buiteveld, H., Hakvoort, J., & Donze, M. (1994). Optical properties of pure water. In *Ocean*
819 *Optics XII* (pp. 174–183). International Society for Optics and Photonics.
- 820 Darvishzadeh, R., Atzberger, C., Skidmore, A., & Schlerf, M. (2011). Mapping grassland
821 leaf area index with airborne hyperspectral imagery: A comparison study of statistical
822 approaches and inversion of radiative transfer models. *ISPRS Journal of Photogrammetry*
823 *and Remote Sensing*, *66*, 894–906.
- 824 Dekker, A. G., Phinn, S. R., Anstee, J., Bissett, P., Brando, V. E., Casey, B., Fearn, P.,
825 Hedley, J., Klonowski, W., Lee, Z. P. et al. (2011). Intercomparison of shallow water
826 bathymetry, hydro-optics, and benthos mapping techniques in Australian and Caribbean
827 coastal environments. *Limnology and Oceanography: Methods*, *9*, 396–425.
- 828 Drusch, M., Del Bello, U., Carlier, S., Colin, O., Fernandez, V., Gascon, F., Hoersch, B., Isola,
829 C., Laberinti, P., Martimort, P. et al. (2012). Sentinel-2: ESA’s optical high-resolution
830 mission for GMES operational services. *Remote Sensing of Environment*, *120*, 25–36.
- 831 Fearn, P., Klonowski, W., Babcock, R., England, P., & Phillips, J. (2011). Shallow water
832 substrate mapping using hyperspectral remote sensing. *Continental Shelf Research*, *31*,
833 1249–1259.
- 834 Garcia, R. A., Fearn, P. R., & McKinna, L. I. (2014a). Detecting trend and seasonal changes
835 in bathymetry derived from HICO imagery: A case study of shark bay, western australia.
836 *Remote Sensing of Environment*, *147*, 186–205.
- 837 Garcia, R. A., Hedley, J. D., Tin, H. C., & Fearn, P. R. (2015). A method to analyze

838 the potential of optical remote sensing for benthic habitat mapping. *Remote Sensing*, 7,
839 13157–13189.

840 Garcia, R. A., McKinna, L. I., Hedley, J. D., & Fearn, P. R. (2014b). Improving the
841 optimization solution for a semi-analytical shallow water inversion model in the presence
842 of spectrally correlated noise. *Limnol. Oceanogr. Methods*, 12, 651–669.

843 Giardino, C., Candiani, G., Bresciani, M., Lee, Z., Gagliano, S., & Pepe, M. (2012).
844 BOMBER: A tool for estimating water quality and bottom properties from remote sensing
845 images. *Computers & Geosciences*, 45, 313–318.

846 Gillis, D. B., Bowles, J. H., & Moses, W. J. (2013). Improving the retrieval of water inherent
847 optical properties in noisy hyperspectral data through statistical modeling. *Optics express*,
848 21, 21306–21316.

849 Goodman, J., & Ustin, S. L. (2007). Classification of benthic composition in a coral reef
850 environment using spectral unmixing. *Journal of Applied Remote Sensing*, 1, 011501–
851 011501.

852 Goodman, J. A., Lee, Z., & Ustin, S. L. (2008). Influence of atmospheric and sea-surface
853 corrections on retrieval of bottom depth and reflectance using a semi-analytical model: a
854 case study in Kaneohe Bay, Hawaii. *Applied Optics*, 47, F1–F11.

855 Guanter, L., Kaufmann, H., Segl, K., Foerster, S., Rogass, C., Chabrillat, S., Kuester, T.,
856 Hollstein, A., Rossner, G., Chlebek, C. et al. (2015). The EnMAP spaceborne imaging
857 spectroscopy mission for earth observation. *Remote Sensing*, 7, 8830–8857.

858 Hedley, J., Harborne, A., & Mumby, P. (2005). Technical note: Simple and robust removal
859 of sun glint for mapping shallow-water benthos. *International Journal of Remote Sensing*,
860 26, 2107–2112.

861 Hedley, J., Roelfsema, C., Koetz, B., & Phinn, S. (2012a). Capability of the Sentinel-2
862 mission for tropical coral reef mapping and coral bleaching detection. *Remote Sensing of
863 Environment*, 120, 145–155.

- 864 Hedley, J., Roelfsema, C., & Phinn, S. R. (2009). Efficient radiative transfer model inversion
865 for remote sensing applications. *Remote Sensing of Environment*, *113*, 2527–2532.
- 866 Hedley, J. D., Roelfsema, C. M., Phinn, S. R., & Mumby, P. J. (2012b). Environmental and
867 sensor limitations in optical remote sensing of coral reefs: Implications for monitoring and
868 sensor design. *Remote Sensing*, *4*, 271–302.
- 869 Hochberg, E. J., & Atkinson, M. J. (2003). Capabilities of remote sensors to classify coral,
870 algae, and sand as pure and mixed spectra. *Remote Sensing of Environment*, *85*, 174–189.
- 871 Hochberg, E. J., Atkinson, M. J., & Andréfouët, S. (2003). Spectral reflectance of coral reef
872 bottom-types worldwide and implications for coral reef remote sensing. *Remote Sensing
873 of Environment*, *85*, 159–173.
- 874 Jay, S., & Guillaume, M. (2011). Estimation of water column parameters with a maximum
875 likelihood approach. In *Hyperspectral Image and Signal Processing: Evolution in Remote
876 Sensing (WHISPERS), 2011 3rd Workshop on* (pp. 1–4). IEEE.
- 877 Jay, S., & Guillaume, M. (2014). A novel maximum likelihood based method for mapping
878 depth and water quality from hyperspectral remote-sensing data. *Remote Sensing of En-
879 vironment*, *147*, 121–132.
- 880 Jay, S., & Guillaume, M. (2016). Regularized estimation of bathymetry and water quality
881 using hyperspectral remote sensing. *International Journal of Remote Sensing*, *37*, 263–289.
- 882 Jay, S., Guillaume, M., & Blanc-Talon, J. (2012). Underwater target detection with hyper-
883 spectral data: Solutions for both known and unknown water quality. *Selected Topics in
884 Applied Earth Observations and Remote Sensing, IEEE Journal of*, *5*, 1213–1221.
- 885 Jay, S., Maupas, F., Bendoula, R., & Gorretta, N. (2017). Retrieving LAI, chlorophyll and
886 nitrogen contents in sugar beet crops from multi-angular optical remote sensing: com-
887 parison of vegetation indices and PROSAIL inversion for field phenotyping. *Field Crops
888 Research*, *210*, 33–46.

889 Joshi, I., & D'Sa, E. J. (2015). Seasonal variation of colored dissolved organic matter in
890 Barataria Bay, Louisiana, using combined Landsat and field data. *Remote Sensing*, *7*,
891 12478–12502.

892 Klonowski, W. M., Fearn, P. R., & Lynch, M. J. (2007). Retrieving key benthic cover
893 types and bathymetry from hyperspectral imagery. *Journal of Applied Remote Sensing*,
894 *1*, 011505–011505.

895 Knudby, A., Ahmad, S. K., & Ilori, C. (2016). The potential for Landsat-based bathymetry
896 in Canada. *Canadian Journal of Remote Sensing*, *42*, 367–378.

897 Kutser, T., Dekker, A. G., & Skirving, W. (2003). Modeling spectral discrimination of
898 great barrier reef benthic communities by remote sensing instruments. *Limnology and*
899 *Oceanography*, *48*, 497–510.

900 Lee, Z., & Carder, K. L. (2002). Effect of spectral band numbers on the retrieval of water
901 column and bottom properties from ocean color data. *Applied Optics*, *41*, 2191–2201.

902 Lee, Z., Carder, K. L., Chen, R. F., & Peacock, T. G. (2001). Properties of the water column
903 and bottom derived from Airborne Visible Infrared Imaging Spectrometer (AVIRIS) data.
904 *Journal of Geophysical Research: Oceans*, *106*, 11639–11651.

905 Lee, Z., Carder, K. L., Mobley, C. D., Steward, R. G., & Patch, J. S. (1998). Hyperspectral
906 remote sensing for shallow waters. i. a semianalytical model. *Applied Optics*, *37*, 6329–
907 6338.

908 Lee, Z., Carder, K. L., Mobley, C. D., Steward, R. G., & Patch, J. S. (1999). Hyperspectral
909 remote sensing for shallow waters: 2. deriving bottom depths and water properties by
910 optimization. *Applied Optics*, *38*, 3831–3843.

911 Lee, Z., Weidemann, A., & Arnone, R. (2013). Combined effect of reduced band number and
912 increased bandwidth on shallow water remote sensing: The case of Worldview 2. *IEEE*
913 *Transactions on Geoscience and Remote Sensing*, *51*, 2577–2586.

914 Manolakis, D., Marden, D., & Shaw, G. A. (2003). Hyperspectral image processing for
915 automatic target detection applications. *Lincoln laboratory journal*, *14*, 79–116.

- 916 Maritorena, S., Morel, A., & Gentili, B. (1994). Diffuse reflectance of oceanic shallow waters:
917 Influence of water depth and bottom albedo. *Limnology and Oceanography*, *39*, 1689–1703.
- 918 McKinna, L. I., Fearn, P. R., Weeks, S. J., Werdell, P. J., Reichstetter, M., Franz, B. A.,
919 Shea, D. M., & Feldman, G. C. (2015). A semianalytical ocean color inversion algorithm
920 with explicit water column depth and substrate reflectance parameterization. *Journal of*
921 *Geophysical Research: Oceans*, *120*, 1741–1770.
- 922 Melgani, F., & Bruzzone, L. (2004). Classification of hyperspectral remote sensing images
923 with support vector machines. *IEEE Transactions on geoscience and remote sensing*, *42*,
924 1778–1790.
- 925 Mishra, D., Narumalani, S., Rundquist, D., & Lawson, M. (2006). Benthic habitat mapping
926 in tropical marine environments using QuickBird multispectral data. *Photogrammetric*
927 *Engineering & Remote Sensing*, *72*, 1037–1048.
- 928 Mobley, C. D. (1994). *Light and water: radiative transfer in natural waters*. Academic press.
- 929 Mobley, C. D., Sundman, L. K., Davis, C. O., Bowles, J. H., Downes, T. V., Leathers, R. A.,
930 Montes, M. J., Bissett, W. P., Kohler, D. D., Reid, R. P. et al. (2005). Interpretation of
931 hyperspectral remote-sensing imagery by spectrum matching and look-up tables. *Applied*
932 *Optics*, *44*, 3576–3592.
- 933 Morel, A. (1974). Optical properties of pure water and pure sea water. *Optical aspects of*
934 *oceanography*, *1*, 1–24.
- 935 Mouroulis, P., Van Gorp, B., Green, R. O., Dierssen, H., Wilson, D. W., Eastwood, M.,
936 Boardman, J., Gao, B.-C., Cohen, D., Franklin, B. et al. (2014). Portable Remote Imaging
937 Spectrometer coastal ocean sensor: Design, characteristics, and first flight results. *Applied*
938 *optics*, *53*, 1363–1380.
- 939 Palmason, J. A., Benediktsson, J. A., Sveinsson, J. R., & Chanussot, J. (2005). Classification
940 of hyperspectral data from urban areas using morphological preprocessing and independent
941 component analysis. In *Geoscience and Remote Sensing Symposium, 2005. IGARSS'05.*
942 *Proceedings. 2005 IEEE International* (pp. 4–pp). IEEE volume 1.

- 943 Petit, T., Bajjouk, T., Mouquet, P., Rochette, S., Vozel, B., & Delacourt, C. (2017). Hy-
944 perspectral remote sensing of coral reefs by semi-analytical model inversion—comparison of
945 different inversion setups. *Remote Sensing of Environment*, *190*, 348–365.
- 946 Richter, R. (2012). *Atmospheric / topographic correction for airborne imagery: ATCOR-4*
947 *User Guide*. Wessling, Germany: DLR IB 565-02/11.
- 948 Smet, S., Sicot, G., & Lennon, M. (2010). *Evaluation des capacités de le télédétection hy-*
949 *perspectrale et développement de méthodes innovantes de traitement d’images pour des*
950 *applications Défense en zone littorale (HypLitt)*. Technical Report , contrat de recherche
951 DGA 2010 34 0014.
- 952 Verrelst, J., Camps-Valls, G., Muñoz-Mari, J., Rivera, J. P., Veroustraete, F., Clevers, J. G.,
953 & Moreno, J. (2015). Optical remote sensing and the retrieval of terrestrial vegetation bio-
954 geophysical properties—a review. *ISPRS Journal of Photogrammetry and Remote Sensing*,
955 *108*, 273–290.
- 956 Wettle, M., Brando, V. E., & Dekker, A. G. (2004). A methodology for retrieval of environ-
957 mental noise equivalent spectra applied to four hyperion scenes of the same tropical coral
958 reef. *Remote Sensing of Environment*, *93*, 188–197.
- 959 Willmott, C. J., & Matsuura, K. (2005). Advantages of the mean absolute error (MAE)
960 over the root mean square error (RMSE) in assessing average model performance. *Climate*
961 *research*, *30*, 79–82.